nature communications

Article

https://doi.org/10.1038/s41467-025-59644-y

Endothelial major vault protein alleviates vascular remodeling via promoting Parkin-mediated mitophagy

Received: 23 June 2024

Accepted: 30 April 2025

Bin Jiang[1,5] ✉, Fan Bai[1,5], Yunfu Hu[1,5], Yu Ren[1], Yuan Su[1], Wanxuan Song[1], Kunxin Xie[1], Dongdong Wang[1], Junlu Pan[1], Yuying Liu[1], Yuxin Feng[2], Xiaoyu Li[1], Hanwen Zhang[1], Xudong Zhu[1], Hui Bai[1], Qing Yang[1], Jingjing Ben[1,3] ✉ & Qi Chen[1,4] ✉

Many important vascular diseases including neointimal hyperplasia and atherosclerosis are characterized by the endothelial cell (EC) injury-initiated pathological vascular remodeling. However, the endogenous regulatory mechanisms underlying it are not fully understood. The present study investigates regulatory role of major vault protein (MVP) in the pathogenesis of vascular remodeling via controlling EC injury. By generating male murine vascular disease models, we find that ablation of endothelial MVP increases neointima formation and promotes atherosclerosis. Mechanistically, MVP directly binds with Parkin and inhibits the ubiquitination and proteasomal degradation of Parkin by dissociating the E3 ligase NEDD4L from Parkin, leading to activation of Parkin-mediated mitophagy pathway in the EC. Genetic modulation of endothelial MVP and Parkin influences the mitophagy, apoptosis, and neointima formation. These results demonstrate that MVP acts as an intracellular regulator promoting Parkin-mediated mitophagy. Our findings suggest that MVP/NEDD4L/Parkin axis may serve as the therapeutic target for treating intimal hyperplasia and atherosclerosis.

Pathological vascular remodeling is characterized by structural and functional alterations in the vessel wall during the process of multiple vascular diseases including neointimal hyperplasia, atherosclerosis, and pulmonary hypertension. Development of pathological vascular remodeling may lead to arterial stenosis in response to the persistent malignant stimuli or vascular injury, and ultimately to a variety of potentially life-threatening clinical cardiovascular events. Currently, the interventional strategies for both atherosclerosis and neointimal hyperplasia are confined to targeting cardiovascular disease risk factors and surgical modalities, highlighting the importance of deep insights into the mechanisms of pathological vascular remodeling and identification of new targets for therapeutic applications[1].

Endothelial cell (EC) serves as the barrier to blood vessel wall enabling a controlled exchange of fluids, molecules, and cells. Endothelial cell injury is the initiating factor for neointima formation, followed by localized endothelial denudation, an uncontrolled cascade of thrombus formation, proliferation of vascular smooth muscle cells (VSMCs), and infiltration of immune cells in the vessel wall[2,3]. Dysfunction of EC also plays crucial roles in the initiation and progression of atherosclerosis[4]. Causes of endothelial dysfunction include oxidative stress, shear stress, and inflammation, which decrease the

---

[1] Department of Pathophysiology, Key Laboratory of Targeted Intervention of Cardiovascular Disease, Collaborative Innovation Center for Cardiovascular Disease Translational Medicine, Nanjing Medical University, Nanjing, China. [2] Department of Forensic Medicine, Nanjing Medical University, Nanjing, China. [3] The Affiliated Wuxi People's Hospital of Nanjing Medical University, Wuxi People's Hospital, Wuxi Medical Center, Nanjing Medical University, Nanjing, China. [4] The Affiliated Suzhou Hospital of Nanjing Medical University, Suzhou Municipal Hospital, Gusu School, Nanjing Medical University, Nanjing, China. [5] These authors contributed equally: Bin Jiang, Fan Bai, Yunfu Hu. ✉ e-mail: jiangbin@njmu.edu.cn; bjj@njmu.edu.cn; qichen@njmu.edu.cn

bioavailability of nitric oxide. Oxidative stress is induced by most of cardiovascular risk factors, and contributes to one of the most important underlying mechanisms for the endothelial dysfunction-related vascular diseases. Recently, excessive reactive oxygen species (ROS) production by accumulative flawed mitochondria in ECs attracts great attention. Mitophagy is a special form of autophagy functioning in selective elimination of dysfunctional mitochondria. It maintains healthy mitochondrial and cell survival[5,6]. Defective mitophagy in ECs accelerates the accumulation of dysfunctional mitochondria and triggers oxidative stress, leading to apoptosis[7,8]. However, the detailed regulatory mechanisms of mitophagy are not fully understood. Identification of pivotal regulatory nodes in the mitophagy pathway is important for maintenance of intracellular homeostasis in the stressed vascular ECs.

Major vault protein (MVP) is the predominant component of cellular vaults involving in diverse biological processes including multidrug resistance, nuclear pore assembly, signal transduction, and immune response[9–11]. It also participates in the regulation of vascular cell survival. For example, MVP cooperates with Ras for optimal epidermal growth factor (EGF)-induced Elk-1 activation that is required for fibroblast survival[12]. Coincidentally, MVP alleviates SMC apoptosis and promotes cell survival by binding to myosin heavy chain 9 (MYH9)[13]. MVP has been found to alleviate doxorubicin-induced cardiac dysfunction, oxidative stress, and fibrosis via activating AKT signaling and inhibiting cardiomyocyte apoptosis[14]. MVP in macrophages and ECs inhibits inflammation by suppressing nuclear factor kappa B (NF-κB)/c-Jun N-terminal kinase (JNK) signaling pathways, and attenuates atherosclerosis formation and development[15–17]. However, the functional involvements of MVP in EC mitochondrial biology and mitophagy are not clear.

In this study, we identify MVP as a regulator for Parkin-mediated mitophagy in ECs. The MVP/neuronal precursor cell-expressed developmentally down-regulated 4 like (NEDD4L)/Parkin axis promotes endothelial mitophagy and cell survival, thereby antagonizing neointimal hyperplasia and atherosclerosis in mice. Our findings reveal that MVP may represent an attractive therapeutic target for treatment of vascular remodeling.

Results

Endothelial MVP is up-regulated in vascular diseases

To investigate the role of major vault protein (MVP) in vascular diseases, we examined its expression in human carotid arteries by performing immunohistochemical staining (IHC). We found that MVP was up-regulated in carotid atherosclerotic plaques compared to the arteries without plaques (Fig. 1A). This finding is consistent with the public data of human Gene Expression Omnibus (GEO) databases, in which a higher expression of MVP was in carotid plaques compared to control arteries (GSE100927 and GSE43292) (Fig. 1B, C). The expressional level of MVP in the advanced plaques was also higher than that in the early-stage lesions (GSE28829, Fig. 1D). When the top 5000 genes expressed in GSE28829 were subjected to the weighted gene co-expression network analysis (WGCNA) using the R package, two modules with the highest correlation with MVP expression were identified (Fig. 1E). One was associated with endocytosis, inflammatory response, and macrophage activation pathways, which is consistent with previous discoveries (Fig. 1F)[15–17]. Another functional covariance module, of note, was on vascular structure, angiogenesis, endothelial cell (EC) migration, and apoptosis, which is closely related to EC functions (Fig. 1G). The WGCNA of GSE100927 acquired similar results (Supplementary Fig. 1A, B). These results suggest that MVP in atherosclerosis may involve diverse EC functions.

We next determined the expression of endothelial MVP in the atherosclerotic model generated by feeding 8-week-old male *Apoe*$^{-/-}$ mice a Western diet (WD) for 12 weeks. Immunofluorescence (IF) staining revealed that WD feeding increased MVP expression in both CD31$^+$ endothelial cells and CD31$^-$ cells in the aortic root (Fig. 1H). We also examined endothelial MVP in the male mouse neointimal model by left common carotid artery ligation, wherein the non-ligated right common carotid artery served as a sham-operated artery. Western blot showed that MVP expression in the ligated arteries was increased (Fig. 1I). IF staining confirmed that the up-regulated MVP was predominantly in CD31$^+$ ECs of ligated arteries (Fig. 1J). When human umbilical vein endothelial cells (HUVECs) and aortic endothelial cells (HAECs) were isolated and cultured in vitro respectively, the cellular MVP level increased upon the tumor necrosis factor (TNF)-α stimulation (Supplementary Fig. 1C, D). These results indicate that endothelial MVP is up-regulated in vascular diseases.

Endothelial MVP ameliorates neointimal hyperplasia and vascular remodeling

We next used a tamoxifen-inducible endothelial *Mvp*-knockout mouse model (*Mvp*^{ECKO}) to determine the impact of MVP on vascular diseases (Supplementary Fig. 2A, B). There was no detectable MVP in mouse aortic ECs (MAECs) of the tamoxifen-administrated *Mvp*^{ECKO} mice (Supplementary Fig. 2C, D). After 4 weeks of the left common carotid artery ligation (Fig. 2A), male *Mvp*^{ECKO} mice displayed 56% increase in neointima area, 109% increase in the intima-to-media ratio (I/M ratio), and 61% increase in stenosis compared to *Mvp*^{ECWT} littermates, respectively. Ablation of endothelial MVP did not alter the medial and overall vessel areas in the ligated artery (Fig. 2B, C).

We also generated inducible *Mvp*^{ECKO}*Apoe*$^{-/-}$ mice by crossing *Mvp*^{ECKO} mice with *Apoe*$^{-/-}$ mice to examine the role of endothelial MVP in male murine atherosclerotic model (Fig. 2D, Supplementary Fig. 2E). Ablation of endothelial MVP did not alter the plasma levels of cholesterol and triglycerides after 14 weeks of WD feeding (Fig. 2E). However, it increased atherosclerotic lesions as measurements of aortic *en face* Oil Red O-positive staining area (Fig. 2F). Morphological analysis of the aortic roots showed the increased atherosclerotic lesion area (by 27%) and lipid accumulation (by 55%) in *Mvp*^{ECKO}*Apoe*$^{-/-}$ mice compared to those of *Mvp*^{ECWT}*Apoe*$^{-/-}$ mice, respectively (Fig. 2G, H). It was accompanied with 103% increase in necrotic core area instead of collagen content (Fig. 2I, J). Consistently, IF staining of aortic roots displayed 59% increase in the CD68$^+$ macrophages and 38% decrease in the alpha smooth muscle actin (α-SMA)$^+$ smooth muscle cells (SMCs) in the WD-fed *Mvp*^{ECKO}*Apoe*$^{-/-}$ mice (Fig. 2K, L). These results demonstrate that endothelial MVP deficiency accelerates atherosclerosis development.

The role of endothelial MVP in the pulmonary vascular remodeling was determined using male murine hypoxia-induced pulmonary hypertension (PH) model (Supplementary Fig. 2F). No significant difference in the basal right ventricle systolic pressure (RVSP) was observed between *Mvp*^{ECWT} and *Mvp*^{ECKO} mice under normoxia conditions (Supplementary Fig. 2G). Following 3 weeks of hypoxia (10% O_2), endothelial MVP ablation increased RVSP from 27.6 ± 2.9 mmHg to 35.7 ± 2.6 mmHg (Supplementary Fig. 2G). The RV/Left Ventricule +Septum (RV/LV + S) weight ratio, an indicator of RV hypertrophy, increased in *Mvp*^{ECKO} mice (Supplementary Fig. 2H). H&E and α-SMA staining showed that endothelial MVP deficiency exacerbated the occlusion of pulmonary arterioles (Supplementary Fig. 2I–K). These data indicate that endothelial MVP deficiency aggravates pulmonary artery (PA) remodeling and PH.

Endothelial MVP deficiency induces changes in the neointima cell composition and phenotype

To characterize the influence of endothelial MVP deficiency on the artery ligation-induced changes in cell composition and phenotype, we performed single-cell RNA sequencing (scRNA-seq) of 13,835 cells in the isolated carotid arteries, 7327 ones from *Mvp*^{ECWT} and 6508 ones from *Mvp*^{ECKO} mice, at 28 days post ligation (Fig. 3A). Canonical marker expression-based clustering algorithms yielded 17 distinct clusters

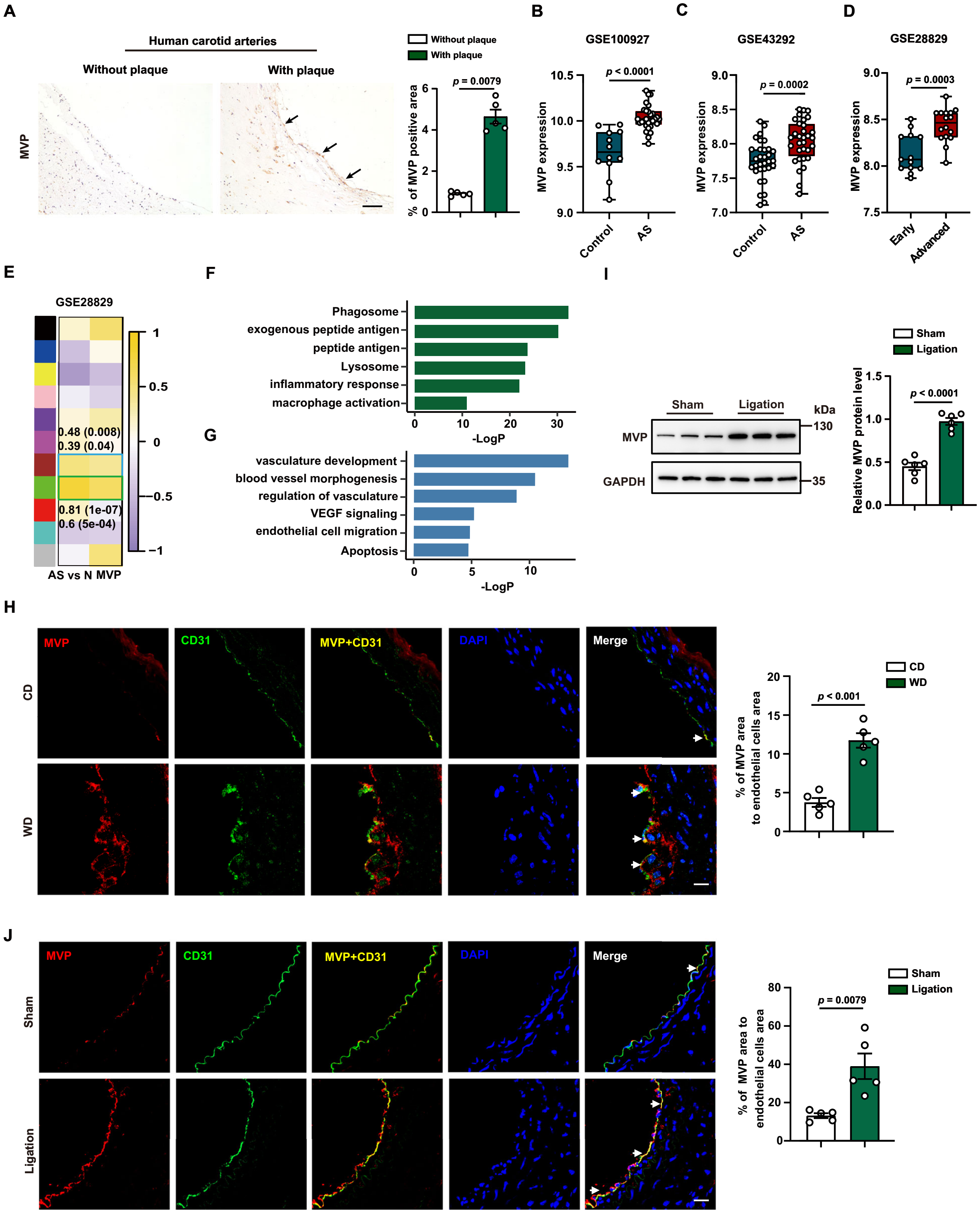

covering 10 major types of cells (Fig. 3B, C, Supplementary Fig. 3A, B). Knockout of endothelial MVP led to a change in cell proportion, in which SMC abundance increased the most obviously from 9% in *Mvp*^{ECWT} mice to 13.8% in *Mvp*^{ECKO} mice (Fig. 3D, E). Moreover, ablation of endothelial MVP resulted in a significant change in the proportion of three distinct SMC subpopulations (Fig. 3F). Both Cluster SMC1, predominant expression of the SMC differentiation genes such as *Acta2*, *Mylk*, and *Tagln* and annotated as differentiated SMCs, and Cluster SMC2, moderately enriched in differentiation genes and *Ly6a*, *Vcam1*, and *Cxcl12* genes and defined as intermediate cell state (ICS) of SMCs[18], decreased from 52.0% to 46.1% and from 47.6% to 42.3%, respectively. Cluster SMC3, mainly expressing osteoblast differentiation-associated genes as *Spp1*, *Sox9*, and *Col2a1* and annotated as chondrocyte-like SMCs[18,19], dramatically increased from 0.4% to 11.6% by endothelial MVP knockout (Fig. 3G, H, Supplementary Fig. 3C). The pseudotime analysis confirmed that SMCs experienced an organized progression from SMC1 to SMC3, via SMC2, by endothelial MVP deficiency (Supplementary Fig. 3D–F). These results suggest that endothelial MVP

Fig. 1 | Endothelial MVP expression is up-regulated in vascular diseases. **A** Immunohistochemical staining and quantification of MVP in human carotid arteries with or without plaques ($n = 5$). Scale bars = 50 µm. **B** Box plot of MVP expression data from human carotid artery plaques ($n = 29$) and healthy controls ($n = 12$) in Gene Expression Omnibus (GEO) dataset GSE100927. **C** Box plot of MVP expression data from human carotid artery lesions and healthy group in GEO dataset GSE43292 ($n = 32$). **D** Box plot of MVP expression data from human carotid artery lesions classified as early plaque ($n = 13$) and advanced plaque ($n = 16$) in GEO dataset GSE28829. **E** Weighted gene co-expression network analysis (WGCNA) of the top 5000 gene expressions in GEO dataset GSE28829 by constructing a scale-free co-expression network. Various colors represent distinct co-expression modules. The top 2 co-expression modules with MVP are marked in green (**F**) and blue (**G**), respectively. **F** Gene Ontology (GO) enrichment analysis of pivotal genes, labeled as green in (**E**), in GEO dataset GSE28829 (Fisher's exact test). **G** GO enrichment analysis of genes, labeled as blue in (**E**), in GEO dataset GSE28829 (Fisher's exact test). **H** Eight-week-old male *Apoe*$^{-/-}$ mice were fed a Western diet (WD) for 12 weeks. Immunofluorescence staining of MVP (red) and CD31 (green) in the atherosclerotic roots of CD-fed or WD-fed mice. Nuclei were stained with DAPI (blue). Quantification of the percentage of MVP area in total endothelial cells (ECs) ($n = 5$). Scale bars = 20 µm. **I, J** Eight-week-old male C57BL/6 J mice underwent ligation operations in the left common carotid arteries. The non-ligated right common carotid arteries served as sham-operated arteries. **I** Western blot analysis of MVP expression in murine carotid arteries with or without ligation after 7 days ($n = 6$). **J** Immunofluorescence staining of MVP (red) and CD31 (green) in the sham and ligated murine arteries harvested after 7 days of ligation. Nuclei were stained with DAPI (blue). Quantification of the percentage of MVP area in total ECs ($n = 5$). Scale bars = 20 µm. Data are presented as mean ± SEM. Statistical significances are assessed by Mann-Whitney test (**A, B**, and **J**) or two-tailed Student's *t*-test (**C, D, H** and **I**). Box plots in (**B**–**D**) spanning from the first to the third quartile, marking the median with a distinct line. The whiskers reach out to the extreme maximum and minimum data point. ns, no significance. Source data are provided as a Source Data file.

deficiency may promote SMC phenotypic transition to the chondrocyte-like cells in the context of neointima formation.

The heterogeneity of ECs was also analyzed by a re-clustering of the EC cohort (Cluster 7), in which four distinct subpopulations (EC1, EC2, EC3, and EC4) were identified (Fig. 3I, J). Cluster EC1, enriched in fibroblast genes (*Fn1*, *Dcn*, and *Col5a2*) and annotated as fibroblast-like ECs[20,21], increased in the *Mvp*^{ECKO} mice. Both Cluster EC2, enriched in lipid metabolism regulatory genes (*Fabp4* and *Cd36*) with a functional specialization in lipid uptake and metabolism, and Cluster EC4, expressing *Lyve1* gene and defined as lymphoid ECs[20], did not show obvious change in proportion by endothelial MVP ablation. Cluster EC3, enriched in transcripts of immediate early genes (IEGs) including *Fosb*, *Fos*, and *Id2* that represents an artifact of single-cell dissociation[22,23], decreased (Fig. 3K, Supplementary Fig. 3G). Of note, the absence of MVP increased endothelial apoptosis as indicated by increasing expression of apoptotic genes such as *Bcl2l11* and *Ecscr* (Fig. 3L). The pathway "positive regulation of endothelial cell apoptosis process" was enriched in the upregulated genes of ECs (Fig. 3M). As such, endothelial MVP deficiency may exacerbate ligation-induced endothelial cell apoptosis and transdifferentiation to fibroblast-like cells, extracellular matrix (ECM) remodeling, and SMC proliferation.

MVP inhibits endothelial apoptosis in murine vascular diseases

Given the important impact of endothelial MVP on vascular homeostasis, we further investigated the role of MVP at the early stage of vascular remodeling. ScRNA-seq analysis of the carotid arteries ligated for 7 days revealed that endothelial MVP ablation led to upregulation of apoptotic genes including *Birc5, Akt1*, and *Nras* (Fig. 4A, Supplementary Fig. 4A–C), and "apoptosis" was the most enriched gene ontology (GO) terms in the upregulated endothelial genes (Fig. 4B). In accordance to the discovery by scRNA-seq of the ligated arteries in *Mvp*^{ECKO} mice, whole transcriptome RNA sequencing (RNA-seq) of cultured HUVECs showed that MVP knockdown by transfection of the lentivirus vector bearing MVP short hairpin RNA (shRNA) rendered the apoptosis pathway one of the top 5 enriched pathways (Fig. 4C–E). Flow cytometry of the Annexin V/PI stained-ECs confirmed the aggravated effect of MVP knockdown on the TNF-α-induced endothelial apoptosis (Fig. 4F, G, Supplementary Fig. 4D–G). In addition, MVP knockdown elevated the TNF-α-induced pro-apoptotic protein cleaved-Caspase3 in cells and increased the number of terminal deoxynucleotidyl transferase dUTP nick-end labeling (TUNEL)-positive cells (Fig. 4H, I, Supplementary Fig. 4H, I). These in vitro observations were corroborated by the in vivo studies that endothelial MVP ablation increased endothelial apoptosis in the ligated carotid artery (Fig. 4J, K) as well as in the aortic wall of WD-fed *Apoe*$^{-/-}$ mice (Fig. 4L, M). Thus, MVP may inhibit endothelial apoptosis in murine vascular diseases.

MVP inhibits oxidative stress by promoting mitophagy in endothelial cells

To understand the mechanism underlying MVP inhibiting endothelial apoptosis, we examined vascular reactive oxygen species (ROS) production in *Mvp*^{ECKO} mice by dihydroethidium (DHE) fluorescence staining. We found that ablation of endothelial MVP increased ROS accumulation in both the ligated arteries (Fig. 5A) and the WD-fed *Apoe*$^{-/-}$ mouse aortas (Fig. 5B). Knockdown of MVP increased TNF-α-induced ROS production in cultured ECs (Fig. 5C, D). Of note, the increased ROS production by MVP knockdown was also found in mitochondria (mitoROS) under confocal microscopic observation (Fig. 5E–H).

The healthy and functional mitochondrial network is critical for cell quality control, and dysfunctional mitochondria constitute a key factor causing ROS accumulation in cells. We next determined whether modulation of intracellular MVP level influences the number and activity of mitochondria in ECs. Staining with Mito-Tracker Green, a marker of mitochondria, showed an aggravated effect of MVP knockdown on the TNF-α-induced increase in mitochondria count in ECs (Supplementary Fig. 5A, B). Consistent with it, the mitochondrial membrane potential (MMP) decreased in the MVP knockdown ECs (Supplementary Fig. 5C, D), suggesting a protective effect of MVP on mitochondrial function. JC-1 staining of ECs confirmed the detrimental effect of endothelial MVP knockout on MMP in the ligated carotid arteries and WD-fed aortas (Fig. 5I, J). These findings were further corroborated by the experimental observation using Mito Q, a mitoROS scavenger. Fig. 5K showed that treatment with Mito Q effectively blocked the lower MVP-induced increase in cleaved-Caspase3 in HUVECs. These results demonstrate that MVP may prevent apoptosis via inhibiting mitoROS accumulation in ECs.

The causal linkage between MVP and mitoROS production as well as mitochondrial homeostasis was further explored by analyzing GO enrichment of genes in the MVP knockdown HUVECs. Fig. 6A showed that mitophagy was the mostly crippled biological process in the mitochondria by MVP knockdown. Intriguingly, down-regulation of MVP did not alter the expression levels of major proteins driving mitochondrial dynamics and biosynthesis, including dynamin-related protein 1 (DRP1), mitofusin1 (MFN1), and PPAR-gamma coactivator 1α (PGC1α), but did inhibit the expression of autophagy marker LC3B-II in cells (Supplementary Fig. 6A). It also led to downregulation of the autophagy/mitophagy-related genes such as *ATG2A*, *ATG4D*, and *ATG4B* in the MVP knockdown HUVECs (Supplementary Fig. 6B), suggesting the involvement of MVP in autophagy/mitophagy.

MVP knockdown inhibited the mitophagy inducer carbonyl cyanide chlorophenylhydrazone (CCCP)-induced cytoplasmic LC3B-II upregulation in HUVECs, HAECs, and human lung microvascular endothelial cells (HLMECs) (Fig. 6B, Supplementary Fig. 6C, D). We also found that the CCCP-induced mitochondria-associated LC3B (mito-

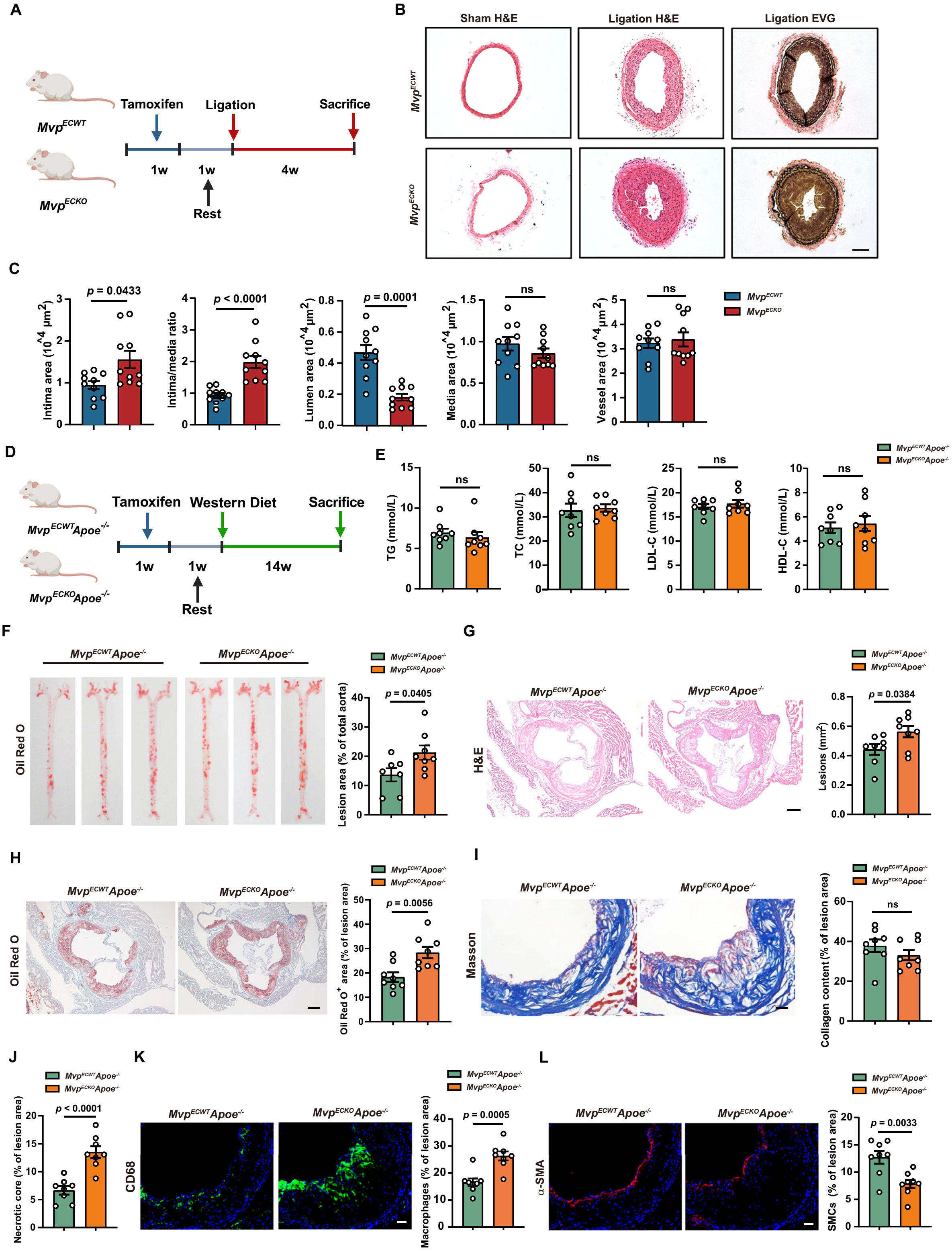

LC3B) was visibly reduced by the MVP knockdown (Fig. 6B, Supplementary Fig. 6C, D). These results were accompanied with the transmission electron microscopy (TEM) observation that MVP knockdown decreased numbers of both mitophagosomes and autolysosomes in the CCCP-treated ECs (Fig. 6C, Supplementary Fig. 6E). The CCCP-induced co-localization of COXIV-positive mitochondria with LC3B was also inhibited by MVP knockdown (Supplementary Fig. 6F, G). The in vivo observations validated that endothelial MVP ablation caused less co-localization of mitochondria with autophagosomes in CD31$^+$ ECs of the ligated arteries (Fig. 6D, E) as well as WD-fed *Apoe*$^{-/-}$ aortas (Fig. 6F, G). MVP re-expression in cultured *Mvp*$^{-/-}$ MAECs rescued the mitophagy (Supplementary Fig. 6H, I).

We then directly measured mitophagic flux in the mt-Keima lentivirus transfected cells. For unstressed cells, mt-Keima manifests green fluorescence. When mitophagosomes fuse with acidified lysosomes to form autolysosomes, mt-Keima manifests red fluorescence[24,25]. We found that Keima dots (red, autolysosomes) were accumulated in the CCCP-treated HUVECs, which was mitigated by

Fig. 2 | Ablation of endothelial MVP aggravates neointimal hyperplasia and atherosclerosis in mice. A Schematic illustration of the experimental design for injection of the tamoxifen and carotid artery ligation of male Mvp^{ECWT} and Mvp^{ECKO} mice. The figure is created using BioRender. Jiang B. (2025) https://BioRender.com/fazni0s. **B** Representative hematoxylin and eosin (H&E) and Elastic Van Gieson (EVG) staining images of non-ligated or ligated carotid arteries 4 weeks post ligation in Mvp^{ECWT} and Mvp^{ECKO} mice. Scale bar, 50 μm. **C** Neointima area, intima to media ratio, lumen area, media area, and vessel area of ligated carotid arteries in Mvp^{ECWT} and Mvp^{ECKO} mice were quantified ($n = 10$). **D** Experimental design for injection of the tamoxifen and WD feeding for 14 weeks in 6-week-old male $Mvp^{ECWT}Apoe^{-/-}$ and $Mvp^{ECKO}Apoe^{-/-}$ mice. The figure is created using BioRender. Jiang B. (2025) https://BioRender.com/ken5vk5. **E** Lipids profiles in $Mvp^{ECWT}Apoe^{-/-}$ and $Mvp^{ECKO}Apoe^{-/-}$ mice after 14 weeks of WD feeding ($n = 8$). **F** Representative images of *en face* Oil Red O staining of whole murine aortas. Quantification of the percentage of plaque area in whole aortas from $Mvp^{ECWT}Apoe^{-/-}$ ($n = 7$) and $Mvp^{ECKO}Apoe^{-/-}$ mice ($n = 8$). **G** Representative H&E staining images of cross-sections of murine aortic roots. Scale bars, 200 μm. Quantification of plaque area in aortic root ($n = 8$). **H** Representative Oil Red O staining images of cross-sections of the aortic root. Scale bars, 200 μm. Quantification of the percentage of Oil Red O staining of plaque area in whole aortic root plaque area ($n = 8$). **I** Representative Masson's trichrome staining images of aortic root sections. Scale bars, 50 μm. Quantification of the percentage of collagen areas in plaques ($n = 8$). **J** Quantification of the percentage of necrotic core in plaques ($n = 8$). **K** Immunofluorescence staining images of CD68-positive macrophages in the aortic root. Scale bars, 50 μm. Quantification of CD68-positive staining of plaque area in aortic root ($n = 8$). **L** Immunofluorescence staining images of α-SMA-positive smooth muscle cells (SMCs) in the aortic root. Scale bars, 50 μm. Quantification of α-SMA positive staining of plaque area in aortic root ($n = 8$). Data are presented as mean ± SEM. Statistical significances are assessed by Mann-Whitney test (**C**, TG and TC in **E**) or two-tailed Student's *t*-test (LDL-C and HDL-C in **E**–**L**). ns, no significance. Source data are provided as a Source Data file.

MVP knockdown (Supplementary Fig. 6J). Consistent results were obtained by intravenous transfection of Lenti-mKeima into either the mice with artery ligation for 7 days (Fig. 6H, I) or the $Mvp^{ECKO}Apoe^{-/-}$ mice fed a WD for 4 weeks (Fig. 6J, K). Lysosome inhibitor bafilomycin A1 (BafA1) blocks mature autophagosomes fusion into lysosomes and subsequent accumulation in cells[26], but it didn't alter the expression pattern of LC3B-II in the MVP knockdown HUVECs (Fig. 6L). These data suggest that MVP may promote mitophagosome formation rather than mitophagosome fusion into lysosome. This hypothesis was verified by the discovery that mitophagy inhibitor cyclosporine A (CsA) could block the anti-apoptotic effect of MVP in HUVECs (Fig. 6M). Thus, our data demonstrate that MVP promotes endothelial mitophagy.

MVP binds with Parkin to prevent NEDD4L-mediated Parkin degradation

To uncover the molecular mechanisms behind MVP regulating mitophagy, we searched for the potential intermediators contributing to the MVP-regulated mitophagy pathway. When the key mitophagy-involved regulative components including PTEN-induced kinase 1 (PINK1), Parkin, BCL2 interacting protein 3 (BNIP3), BCL2 interacting protein 3 like (BNIP3L/NIX), or FUN14 domain-containing 1 (FUNDC1) were co-transfected with MVP into HEK293T cells respectively, we found that MVP could exclusively interact with Parkin by a co-immunoprecipitation (Co-IP) (Fig. 7A, B, Supplementary Fig. 7A–D). IF staining revealed a co-localization of MVP and Parkin in murine and human atherosclerotic plaques (Fig. 7C, D). Consistently, proximity ligation assay (PLA) showed a close association (< 40 nm) between them (Fig. 7E, Supplementary Fig. 7E). The interaction between Parkin and MVP was increased upon CCCP treatment (Fig. 7F), implying a potential impact of this interaction on the Parkin-mediated mitophagy. MVP knockdown decreased Parkin protein level, instead of mRNA level, in the ECs (Fig. 7G, Supplementary Fig. 7F–I). No similar impact was found on other mitophagy-involved regulative components, including BNIP3, NIX, FUNDC1, and PINK1 (Supplementary Fig. 7J).

Treatment with cyclohexane (CHX), a protein synthesis inhibitor, led to a loss of cellular Parkin which was delayed by MVP overexpression (Fig. 7H), suggesting a protein synthesis-independent mechanism underlying MVP's action on intracellular Parkin. Furthermore, MVP silence-induced Parkin down-regulation was attenuated by treatment with proteasomal inhibitor MG132 (Fig. 7I). The ubiquitination of Parkin was also inhibited by the MVP overexpression in HEK293T cells, in which K48-ubiquitination but not K63-ubiquitination of Parkin was selectively suppressed (Fig. 7J, K, Supplementary Fig 7K). MVP knockdown affected Parkin level in cells, thereby inhibiting Parkin translocation to mitochondria and subsequent mitophagy (Fig. 7L). Conversely, MVP re-expression in cultured $Mvp^{-/-}$ MAECs reactivated the CCCP-induced Parkin translocation to mitochondria (Supplementary Fig. 7L, M). Together, these results demonstrate that MVP may maintain Parkin stability via inhibiting its ubiquitin/proteasome-mediated degradation system, and promote Parkin's translocation to mitochondria and subsequent mitophagy.

When UbiBrowser, an integrated bioinformatics platform for predicting proteome-wide E3 substrate networks, was used to search for the potential E3 ligases involved in the proteasomal degradation of Parkin, neuronal precursor cell-expressed developmentally down-regulated 4 (NEDD4), itchy homolog (ITCH), smad ubiquitination regulatory factor 1 (SMURF1), and neuronal precursor cell-expressed developmentally down-regulated 4 like (NEDD4L) were labeled as the candidates of E3 substrate ligases for Parkin (Supplementary Fig. 8A). Among them, NEDD4L exhibited the strongest ability to promote the ubiquitination of Parkin in cells (Supplementary Fig. 8B). It could bind directly with Parkin in cells (Supplementary Fig. 8C). Both IF staining and PLA staining of NEDD4L and Parkin revealed the co-localization between them in murine atherosclerotic plaques (Supplementary Fig. 8D, E). Moreover, NEDD4L promoted the K48-ubiquitination of Parkin, which was blocked by mutation of NEDD4L E3 ligase active site (C942S) (Supplementary Fig. 8F). The pro-degradation of Parkin by NEDD4L was blocked by MG132 treatment (Supplementary Fig. 8G). These data reveal Parkin as a bona fide substrate of NEDD4L. Intriguingly, MVP overexpression inhibited Parkin-NEDD4L interaction and subsequent NEDD4L-mediated Parkin ubiquitination (Fig. 7M, N). Knockdown of NEDD4L restored the MVP silence-induced decrease in cellular Parkin (Fig. 7O). These results indicate that NEDD4L functions as an E3 ligase of Parkin, and MVP competes with NEDD4L for binding to Parkin, thereby strengthening the Parkin stability.

Overexpression of Parkin rescues MVP deficiency-induced vascular remodeling in neointima formation

The roles of endothelial MVP-Parkin axis in mitophagy and apoptosis were further examined in vitro. Overexpression of Parkin significantly ameliorated mitophagy arrest induced by MVP knockdown as measurements of cellular expression of LC3B-II and co-localization of COXIV with LC3B (Fig. 8A, Supplementary Fig. 9A). Parkin overexpression could also reverse the MVP knockdown-aggravated elevation of cleaved-Caspase3 in the TNF-α-treated cells (Fig. 8B). These results demonstrate that Parkin acts as a key intermediator for the MVP-mediated mitophagy in ECs.

Furthermore, we employed the EC-specific intercellular adhesion molecule 2 (ICAM2) promoter-driven adeno-associated virus isotype 9-encoding Parkin (AAV-Parkin) transfection approach to investigate the impact of endothelial MVP-Parkin axis on vascular remodeling in vivo (Fig. 8C). The overexpression efficiency and specificity of endothelial Parkin in Mvp^{ECKO} mice were monitored by IF staining (Supplementary Fig. 9B). Four weeks after ligation, the increased murine neointima area and TUNEL staining of $CD31^{+}$ ECs by endothelial

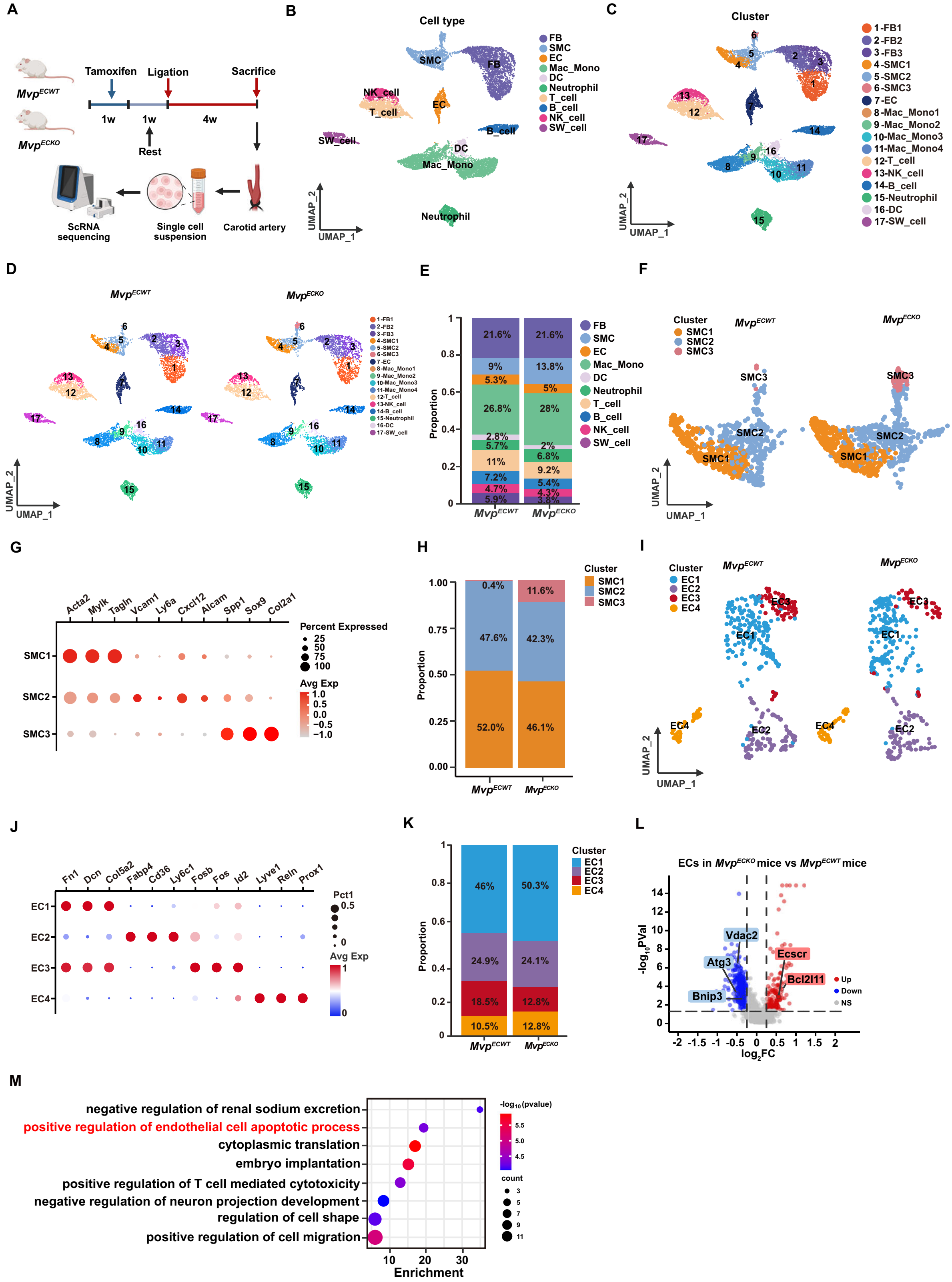

MVP ablation were successfully reversed by overexpression of Parkin in ECs (Fig. 8D–G). Consistently, Parkin overexpression reactivating the mitophagy was evidenced by increased co-localization of mitochondria with autophagosomes in the Mvp^{ECKO} CD31$^+$ ECs (Fig. 8H, I).

We finally studied the translational significance of MVP re-expression in ECs by intravenous transfection of AAV-MVP in Mvp^{ECKO} mice (Fig. 9A, Supplementary Fig. 10A). Forced expression of MVP decreased the ligation-induced neointima formation, intima area, and ratio of intima to media in the carotid arteries, whereas it had minimal effects on the media area (Fig. 9B, C). Notably, MVP re-expression in ECs decreased frequency of TUNEL staining, accompanied by increased intensity of LC3B and COXIV co-staining. All these effects of MVP re-expression were obviously reversed by Parkin knockdown in ECs (Fig. 9D–G, Supplementary Fig. 10B). These results highlight that

Fig. 3 | Endothelial MVP ablation induces changes in neointimal cell proportion and phenotype by single-cell RNA sequencing analysis. A Workflow of single-cell RNA sequencing (scRNA-seq) of cells in the isolated carotid arteries from *Mvp*^{ECWT} and *Mvp*^{ECKO} mice ligated for 28 days. The figure is created using BioRender. Jiang B. (2025) https://BioRender.com/1lshq6d. **B**, **C** Uniform manifold approximation and projection (UMAP) plots illustrating the annotation of cell types (**B**) and clusters (**C**) in single ligated carotid artery cells. **D** UMAP plots revealing distribution of the cell clusters of the *Mvp*^{ECWT} and *Mvp*^{ECKO} mice, respectively. **E** Proportion of annotated cells in the ligated *Mvp*^{ECWT} and *Mvp*^{ECKO} mice. **F** UMAP plots showing three distinct subpopulations of SMCs clustered in colors. **G** Dot plots showing specific marker gene expression in three SMC subpopulations. **H** Proportion of SMC subpopulations in the ligated *Mvp*^{ECWT} and *Mvp*^{ECKO} mice. **I** UMAP plots showing four distinct subpopulations of ECs clustered in colors. **J** Dot plots showing specific marker gene expression in four EC subpopulations. **K** Proportion of EC subpopulations in the ligated *Mvp*^{ECWT} and *Mvp*^{ECKO} mice. **L** Volcano plots of EC marker genes identified by scRNA-seq of carotid arteries ligated for 28 days. DEGs were highlighted in either blue (downregulated) or red (upregulated). Statistical significances are assessed by the Wilcox test (individual group comparison). **M** GO pathway enrichment analysis of the upregulated DEGs in ECs of *Mvp*^{ECKO} mice (Fisher's exact test).

endothelial MVP alleviates neointimal hyperplasia by promoting Parkin-mediated mitophagy and inhibiting apoptosis.

Discussion

Functional integrity of endothelium is a fundamental factor for maintaining vascular homeostasis. When challenged with various stressors, ECs undergo adaptive responses by mobilizing their vital survival systems. Transition from the adaptive response to the dysfunction of endothelium encompasses various nonadaptive alterations, including disturbance in hemostasis, vascular barrier disruption, abnormality in vascular tone and redox balance, inflammatory response, and thrombosis. As an initiating and stimulating factor for atherosclerotic disease, endothelial dysfunction is the earliest measurable functional deterioration of vessel wall with a reversible character. This confers endothelial dysfunction a potential target for intervention of the vascular disease with important clinical implications. Herein, we uncover a previously unrecognized role of MVP in EC injury-induced vascular remodeling. Our discoveries delineate molecular insights by which MVP mitigates proteasome-mediated ubiquitination degradation of Parkin, a key regulator of the damage-induced mitophagy, driving the progress of mitophagy. The MVP-Parkin interaction protects ECs from apoptosis and consequently alleviates the neointima formation and development of atherosclerosis.

Up-regulation of macrophage MVP has been found in atherosclerotic lesions, in which the sequence of amino acids 686–747 exerts key roles in inhibiting inflammation and antagonizing the onset and development of atherosclerosis[15,16]. The pro-inflammatory transcription factor SP-1 and STAT1 can promote MVP expression, explaining the up-regulation of endothelial MVP in atherosclerotic lesions and the ligated arteries[15,27,28]. Both SP-1 and STAT1 are also activated by low-shear stress to mediate EC injury, which may also attribute to the increased expression of MVP in vascular ECs[20,29,30]. In distinctive to a diffuse distribution in atherosclerotic plaques, the up-regulated MVP predominantly distributed in the endothelium of ligated arteries. This feature implies the importance of endothelial MVP in neointima formation, though the association between MVP single nucleotide polymorphisms (SNPs) and CVD risks is unknown. The analysis results of the weighted gene co-expression network in a public dataset reveal that one of the two highest correlation modules with the MVP expression was associated with EC functions. In response to various environmental and intrinsic insults including mechanical stress, ROS, lipids, and inflammatory cytokines, up-regulation of MVP may be induced for maintaining the endothelium homeostasis.

Different from the cells with higher energy demands on ATP supplies, mitochondria in ECs play critical roles in generating ROS and controlling cell death[31]. Our findings that endothelial MVP deficiency resulted in mitoROS accumulation and mitochondrial dysfunction demonstrate the role of MVP in maintaining mitochondrial homeostasis and mitochondrial quality control process. Unexpectedly, MVP regulates the mitophagy instead of mitochondrial fusion, fission, and biogenesis in ECs. The deficient mitophagy caused by MVP ablation leads to the accumulation of poorly functioning mitochondria and endothelial apoptosis, thereby contributing to the neointima formation and atherosclerosis. In atherosclerotic plaques, mitophagy is known to fight apoptosis by degrading damaged mitochondria in ECs, and defective mitophagy accelerates atherosclerosis progress[32,33]. However, over-activation of mitophagy exhibits detrimental effects on ECs by reducing the number of mitochondria and aggravating cell damage[34]. It is accepted that enhanced mitophagy typically represents an early response against the overproduction of mitoROS to mitigate cell injury and apoptosis, while overwhelming or prolonged mitochondrial damage can induce excessive and pathological activation of mitophagy. The MVP-induced mitophagy may act as an adaptive response to prevent the accumulation of impaired mitochondria in ECs, though its definite function in the dynamic of the vascular remodeling warrants further investigation. Also, modulation of mitophagy to a proper degree will achieve to the effective clearance of damaged mitochondria in the stressed ECs and, thus, may be an alternative strategy for intervention of the vascular disease.

Mitophagy pathway internet is finely tuned in the steady state, in which PINK1-Parkin pathway is the most recognized mitophagy pathway[35,36]. Our discoveries reveal that interaction between MVP and Parkin is requisite for the MVP-induced mitophagy in ECs. Binding to MVP impedes the degradation of Parkin and strengthens Parkin stability, which is pivotal for Parkin conveying mitophagy signals. Parkin acts as an active E3 ligase ubiquitinating a number of outer mitochondrial membrane (OMM) substrates. These ubiquitinated proteins are further phosphorylated by PINK1 to recruit more Parkin to mitochondria, thereby forming ubiquitin chains and triggering mitophagy[37,38]. However, the detrimental role of Parkin in cell survival has been reported[39,40]. This dual role in the cell fate keeps Parkin elusive in atherosclerosis pathogenesis. For example, PINK1-Parkin pathway-induced mitophagy is thought to protect mitochondrial integrity and prevent metabolic stress-induced endothelial injury[41]. Lipid-activated eukaryotic initiation factor 2α (eIF2α) induces mitochondrial Lon protease 1 (LONP1) to degrade PINK1 and blocks Parkin-mediated mitophagy, leading to mitochondrial oxidative stress and hyperlipidemia-induced atherosclerosis[42]. On the contrary, nuclear receptor subfamily 4 group A member 1 (NR4A1) promotes Parkin activation via Ca^{2+}/calmodulin-dependent protein kinase II (CaMKII), leading to excessive mitophagy, EC apoptosis, and atherosclerosis formation[39]. PINK1/Parkin-induced mitophagy also stimulates apelin-13-evoked human aortic VSMC proliferation by activating p-AMPKα and exacerbates the progression of atherosclerotic lesions[40]. These conflicting results may be due to the respective stressed microenvironments that reshape the function of Parkin in atherosclerosis. Maintaining the stability of Parkin, a critical signal amplifier, would be important in the PINKI-Parkin regulatory pathway. The post-translational modification of Parkin, especially its own ubiquitination through K48-dependent ubiquitin chain formation, seems to play a key role in it[43]. On the other side, certain ubiquitin ligases or deubiquitinating enzymes as NRDP1, USP33, and MITOL have been documented to regulate the ubiquitination of Parkin[44–46]. In ECs, we identified Parkin as a substrate of NEDD4L. Functioning as an E3 ligase of Parkin, NEDD4L promoted Parkin ubiquitination and degradation. Similar effects of NEDD4L have been discovered on the degradation of PINK1 and ULK1, positioning NEDD4L as a key negative regulator of PINK1-Parkin pathway[47–49]. MVP competes with NEDD4L for binding to Parkin

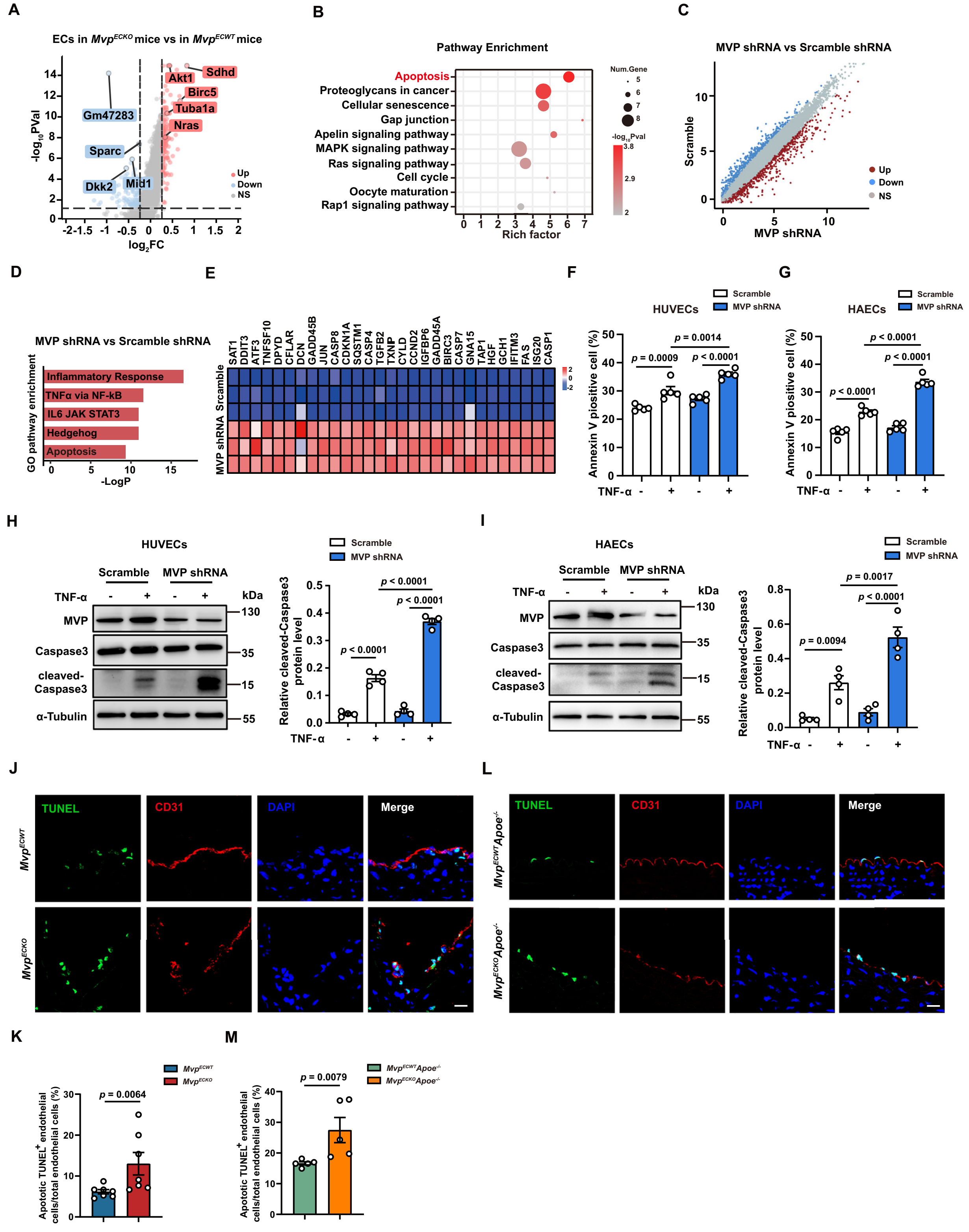

and prevents Parkin degradation. By this mechanism, MVP protects Parkin-mediated mitophagy in ECs and alleviates neointimal hyperplasia and atherosclerosis. Aside from regulating Parkin-induced mitophagy, endothelial MVP seems also promote autophagosome formation since it increased LC3B level. This is consistent with the feature of another component of vault, vtRNA1-1, which participates in the autophagy process by regulating the MAPK/TFEB signaling pathway and inhibiting p62 oligomerization[50,51]. Certainly, the definite role of MVP in autophagy needs further validation.

While the concept of targeting MVP-Parkin axis, for instance through genetical or chemical modulation of MVP/Parkin that can promote the interaction between MVP and Parkin, for translation to clinical outcomes in vascular disease is theoretically conceivable, the researches in humans meet challenges. Especially, the endothelial MVP expression in the unstable atherosclerotic plaques warrants further investigation. The potential side-effects of modulating MVP-Parkin pathway would require extensive further researches.

Fig. 4 | Deficiency of MVP promotes endothelial apoptosis. A Volcano plots of EC marker genes identified by scRNA-seq of carotid arteries ligated for 7 days. Differentially expressed genes (DEGs) were highlighted in either blue (downregulated) or red (upregulated). Statistical significances are assessed by the Wilcox test (individual group comparison). **B** Gene ontology (GO) pathway enrichment analysis of the upregulated DEGs in ECs of *Mvp*^{ECKO} mice (Fisher's exact test). **C** Volcano map of DEGs in the MVP knockdown human umbilical vein endothelial cells (HUVECs) treated by TNF-α (10 μg/ml) for 8 h. Red and blue dots indicate DEGs with a |log2 fold-change | > 1. **D** GO enrichment analysis of the upregulated DEGs in HUVECs transfected by MVP shRNA (Fisher's exact test). **E** Heatmap of the upregulated DEGs associated with positive regulation of apoptosis pathway. **F**, **G** Flow cytometry measurements of Annexin V/PI-positive apoptotic HUVECs (**F**) and human aortic endothelial cells (HAECs, **G**) ($n = 5$, independent biological replicates). **H**, **I** Western blot analysis of Caspase3, cleaved-Caspase3, and MVP protein levels upon MVP knockdown in the TNF-α (10 μg/ml) treated HUVECs (**H**) and HAECs (**I**) ($n = 4$, independent biological replicates). **J** Representative images of terminal deoxynucleotidyl transferase dUTP nick-end labeling (TUNEL) staining of carotid arteries after 7 days of ligation. Scale bars, 20 μm. **K** The percentage of apoptotic ECs in total ECs in the ligated carotid arteries ($n = 7$). **L** Representative images of TUNEL staining of thoracic aortas in *Mvp*^{ECWT}*Apoe*$^{-/-}$ and *Mvp*^{ECKO}*Apoe*$^{-/-}$ mice fed a WD for 4 weeks. Scale bars, 20 μm. **M** Percentage of apoptotic ECs in total ECs in the aortas of the WD-fed mice ($n = 5$). Data are presented as mean ± SEM. Statistical significances are assessed by Mann-Whitney test (**K** and **M**) or one-way ANOVA followed by Tukey post hoc test (**F**–**I**). ns, no significance. Source data are provided as a Source Data file.

In conclusion, our study demonstrates the role of MVP in antagonizing vascular remodeling by activation of Parkin-mediated mitophagy in endothelium (Supplementary Fig. 11). The MVP/NEDD4L/Parkin axis may be potential in prevention and treatment of vascular disease.

Methods

Human samples

Human carotid aortic tissue samples, with or without atherosclerotic plaques, were collected from the patients who underwent carotid endarterectomy ($n = 5$) at the Affiliated Changzhou No. 2 People's Hospital of Nanjing Medical University, Changzhou, China. Written informed consent was obtained from all subjects. All procedures involved human subjects complied with all relevant ethical regulations, were approved by the Ethics Committee of the Affiliated Changzhou No. 2 People's Hospital of Nanjing Medical University (NO. 2023KY018-01), and adhered to the principles of the Declaration of Helsinki. The clinical data of all subjects were summarized in Supplementary table 1. Sex and gender are not relevant for any findings in this study and were therefore not considered in our study design, and participants was not determined based on self-report nor assigned.

Animals

Six-week-old C57BL/6 J and *Apoe*$^{-/-}$ (B6.129P2-*Apoe*^{tm1Unc}/J, 002052) mice were purchased from the Beijing Vital River Laboratory Animal Technology Co., Ltd. (Beijing, China). *Mvp*$^{fl/fl}$ and *Mvp* global knockout (*Mvp*$^{-/-}$) mice were kept in our laboratory. *Cdh5*-Cre^{ERT2} mice were a gift from Prof. Yong Xu (Nanjing Medical University, Nanjing, China). Endothelial-*Mvp* specific knockout (*Mvp*^{ECKO}) mice were generated by crossbreeding *Mvp*$^{fl/fl}$ mice with *Cdh5*-Cre^{ERT2} mice. *Mvp*$^{fl/fl}$ (*Mvp*^{ECWT}) mice served as control. *Mvp*^{ECKO} mice were further mated with *Apoe*$^{-/-}$ mice to generate *Mvp*^{ECKO}*Apoe*$^{-/-}$ mice. Tamoxifen (T5648, Sigma-Aldrich) dissolved in oil was intraperitoneally administered (100 mg/kg) for 7 consecutive days to mice at six weeks of age to activate Cre recombinase. Only male mice were used in this study, since the protective effect of estrogen on atherosclerotic cardiovascular diseases in females. To generate murine vascular disease models, 6-week-old male *Mvp*^{ECWT}, *Mvp*^{ECKO}, *Mvp*^{ECWT}*Apoe*$^{-/-}$, and *Mvp*^{ECKO}*Apoe*$^{-/-}$ mice were used. All mice were kept at ambient temperature (20–24 °C) in humidity-controlled (45–65%) room with a 12 h-light-dark cycle and were allowed free access to water and food in the Model Animal Research Center of Nanjing University. At the terminal of the study, mice were fasted overnight and then euthanized by CO_2 inhalation for blood and tissue sampling. Randomization and blinding were adopted for the animal studies. All animal procedures were conducted following protocols approved by the Institutional Animal Care and Usage Committee of Nanjing Medical University (NO. IACUC-1904031). The experiments outlined in this article conform to the Guide for the Care and Use of Laboratory Animals published by the National Institutes of Health.

Carotid artery ligation and quantification of neointima formation

A well-characterized murine carotid artery ligation was performed as described previously[52,53]. Briefly, one week after tamoxifen treatment, 8-week-old male *Mvp*^{ECKO} and *Mvp*^{ECWT} mice were anesthetized with isoflurane (3%). Left carotid artery was separated and ligated with a 6-0 silk suture just below the carotid bifurcation. The carotid artery on the right side was sham-operated and served as an internal control. Mice were euthanized for analysis of the phenotypic changes. For morphometry experiments, the left and right carotid arteries of mice were harvested, fixed with 4% paraformaldehyde (PFA) overnight, and then embedded in paraffin. Five-μm-thick cross-sections were taken from the artery 0.2 mm from the site of ligation. Specimens were then stained with hematoxylin and eosin (H&E) and Elastic Van Gieson (EVG). The vessel area measurements of the lumen (within the endothelium), the intima (between the endothelium and the internal elastic layer), the media (between the internal elastic layer and the external elastic lamina), and the whole vessel were calculated from 4 serial sections taken every 300 μm using Image-Pro Plus 6.0 software.

Single-cell RNA sequencing (scRNA-seq) and bioinformatic analysis

Left carotid arteries were isolated from male *Mvp*^{ECWT} and *Mvp*^{ECKO} mice at 7 days and 28 days post ligation, respectively. The tissue samples were washed with phosphate-buffered saline (PBS), minced into small pieces, and digested in enzyme solution (450 U/ml collagenase I, 125 U/ml collagenase XI, 60 U/ml hyaluronidase and 60 U/ml DNase I) for 45 min at 37 °C. After digestion, RPMI-1640 containing 10% fetal bovine serum (FBS) was added to the samples to stop the digestion. The resulting cell suspension was obtained through a 70-μm cell strainer to remove undigested tissue mass and washed with PBS containing 0.04% bovine serum albumin (BSA). Dissociated single cells were then stained for viability assessment using Countstar Fluorescence Cell Analyzer.

scRNA-seq experiment was performed by experimental personnel in the laboratory of NovelBio Bio-Pharm Technology (China)[54]. BD Rhapsody system was used to capture the transcriptomic information of the ligated carotid artery-derived single cells. Single-cell capture was achieved by random distribution of a single-cell suspension across >200,000 microwells through a limited dilution approach. Beads with oligonucleotide barcodes were added to saturation so that a bead was paired with a cell in a microwell. The cells were lysed in the microwell to hybridize mRNA molecules to barcoded capture oligos on the beads. Beads were collected into a single tube for reverse transcription and ExoI diaestion. Upon cDNA synthesis, each cDNA molecule was tagged on the 5′ end (that is the 3′ end of a mRNA transcript) with a unique molecular identifier (UMI) and cell barcode indicating its cell origin. Whole transcriptome libraries were prepared using the BD Rhapsody single-cell whole-transcriptom amplification (WTA) workflow, including random priming and extension (RPE), RPE amplification PCR and WTA index PCR. The libraries were quantified using a

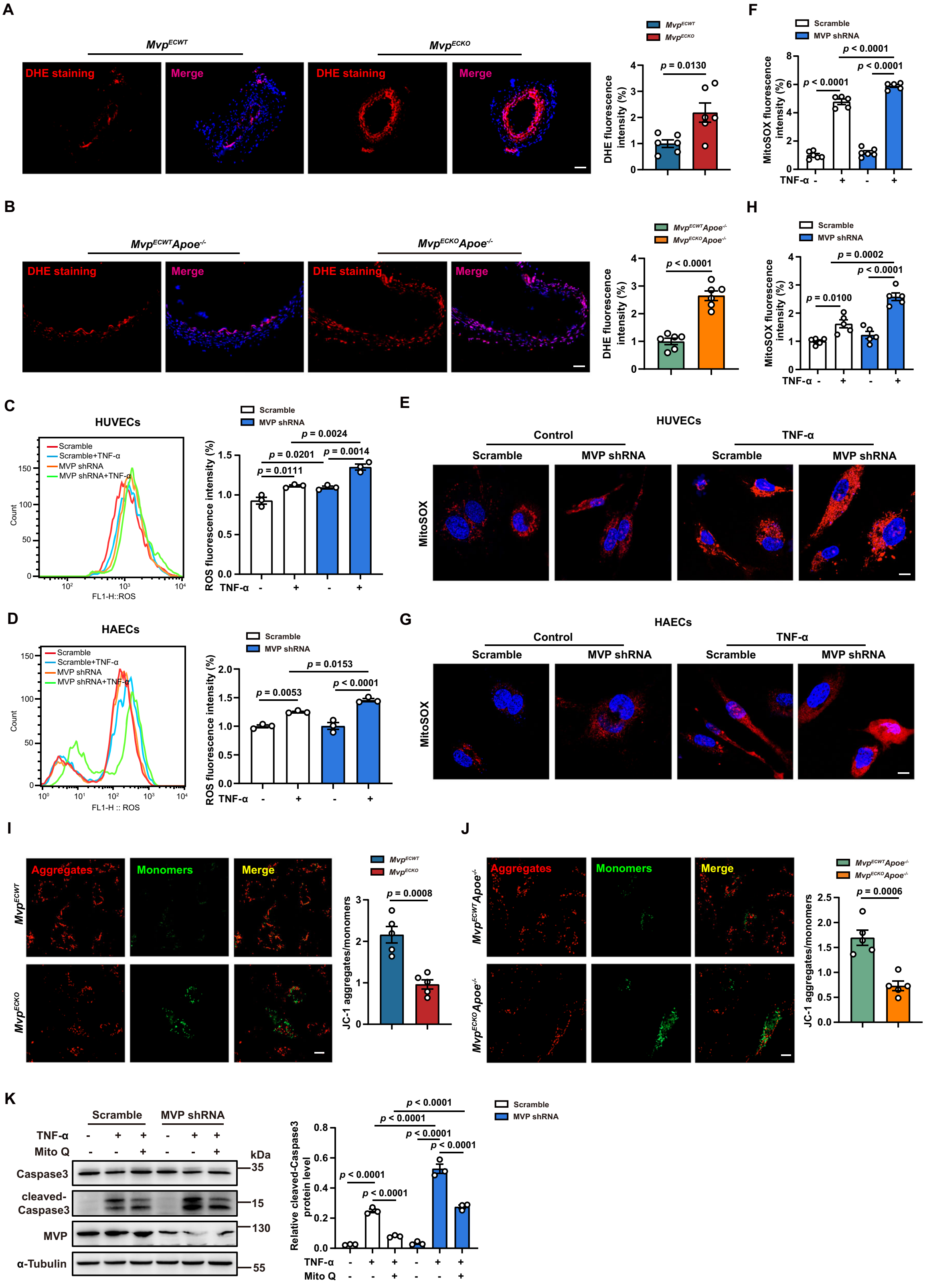

high sensitivity DNA chip (Agilent) on a Bioanalyzer 2200 and the Qubit high sensitivity DNA assay (Thermo Fisher Scientific). Sequencing was performed by BGI T7 (BGI, China) on a 150 bp paired-end run. Data analysis was performed by the NovelBrain Cloud Analysis Platform. As a quality control, cells that expressed gene counts >1000 or <200, and those expressing $>10\%$ mitochondrial UMI counts were removed during the sample preparation.

Adeno-associated virus (AAV)-mediated gene transfer

To achieve endothelial-specific overexpression of MVP and Parkin, adeno-associated virus isotype 9 bearing Flag-tagged MVP or Parkin under the control of the intercellular adhesion molecule 2 (ICAM2) promoter (AAV-MVP or Parkin, 5×10^{11} viral particles per mouse, Shanghai Genechem, China) was intravenously injected into male mice to result in MVP or Parkin overexpression in endothelial cells (ECs).

Fig. 5 | MVP deficiency aggravates oxidative stress and mitochondrial dysfunction in endothelial cells. A Representative fluorescence staining images and quantification of in situ dihydroethidium (DHE) in the carotid arteries of *Mvp*^{ECWT} and *Mvp*^{ECKO} mice after 7 days of ligation ($n = 6$). Scale bar = 50 μm. **B** Representative fluorescence staining images and quantification of in situ DHE in the thoracic aortas of *Mvp*^{ECWT}*Apoe*$^{-/-}$ and *Mvp*^{ECKO}*Apoe*$^{-/-}$ mice after 4 weeks of WD feeding ($n = 6$). Scale bar = 50 μm. (**C** to **H**) Oxidative stress and mitochondrial function upon MVP knockdown in the TNF-α-treated HUVECs and HAECs. **C**, **D** Flow cytometry measurements of intracellular total ROS detected by with DCFH-DA probe in HUVECs (**C**) and HAECs (**D**) ($n = 3$, independent biological replicates). **E**, **F** Representative immunofluorescence staining images (**E**) and quantification (**F**) of MitoSOX in HUVECs (Control group, $n = 6$, independent biological replicates; TNF-α group, $n = 5$, independent biological replicates). Scale bar = 10 μm. (**G, H**) Representative immunofluorescence staining images (**G**) and quantification (**F**) of MitoSOX in HAECs ($n = 5$, independent biological replicates). Scale bar = 10 μm. **I** JC-1 staining of mitochondrial membrane potential in ECs isolated from the carotid arteries after 7 days of ligation ($n = 5$). Scale bar = 10 μm. **J** JC-1 staining of mitochondrial membrane potential in ECs isolated from the aortas after 4 weeks of WD feeding ($n = 5$). Scale bar = 10 μm. **K** Western blot analysis of Caspase3, cleaved-Caspase3, and MVP upon MVP knockdown in the HUVECs treated by TNF-α and Mito Q ($n = 3$, independent biological replicates). Data are presented as mean ± SEM. Statistical significances are assessed by two-tailed Student's t-test (**A**, **B**, **I, J**) or one-way ANOVA followed by Tukey post hoc test (**C**, **D**, **F**, **H**, **K**). ns, no significance. Source data are provided as a Source Data file.

AAV9-Con was used as control. To knock down endothelial Parkin, AAV9-ICAM2-miR30-shParkin (AAV-shParkin) vector was constructed (ViGene Biosciences, China), and AAV9-ICAM2-miR30-shRNA vector inserted by scramble sequence (AAV-sc) was used as a control. One week after AAV delivery, mice were subjected to carotid artery ligation at the indicated time.

Diet-induced atherosclerotic mouse model

The atherosclerotic mouse model was performed and analyzed following the guidelines for experimental atherosclerosis described in the American Heart Association statement[55]. Six-week-old male *Mvp*^{ECKO}*Apoe*$^{-/-}$ and *Mvp*^{ECWT}*Apoe*$^{-/-}$ mice were placed on a Western diet (WD) supplemented with 40% fat and 1.25% cholesterol (D12108C, Research Diets) to develop atherosclerosis after 7 days of tamoxifen induction. After the modeling, mice were fasted overnight and then euthanized by CO_2 inhalation, and atherosclerotic lesions were characterized.

Plasma lipids measurements

Blood samples from WD-fed *Mvp*^{ECKO}*Apoe*$^{-/-}$ and *Mvp*^{ECWT}*Apoe*$^{-/-}$ mice were collected in EDTA-coated tubes, incubated on ice for 30 min, and centrifuged at 1500 g for 20 min at room temperature. The resulting plasma samples were subjected to biochemical analysis for the measurement of plasma triglycerides (TG), total cholesterol (TCH), high-density lipoprotein-cholesterol (HDL-C), and low-density lipoprotein-cholesterol (LDL-C) using the indicated enzymatic assays according to the manufacturer's instructions (JianCheng Bio, China).

Oil Red O staining for atherosclerotic aorta

Six-week-old male *Mvp*^{ECKO}*Apoe*$^{-/-}$ and *Mvp*^{ECWT}*Apoe*$^{-/-}$ mice fed a WD for 14 weeks were euthanized by CO_2 inhalation and perfused with PBS via the left ventricle for 5 min. For *en face* Oil Red O staining of atherosclerotic plaques, aortas were isolated with the removal of connective tissue and the adventitia, and then fixed in 4% PFA overnight. After rinsing with distilled water for 10 min and subsequently with 60% isopropanol, the aortas were stained with Oil Red O (O0625, Sigma-Aldrich) for 15 min and rinsed again in 60% isopropanol and then in distilled water for 10 min. Thereafter, aortas were cut open longitudinally and then photographed with a Canon camera (PowerShot G12, Japan).

Histochemical analysis of atherosclerotic lesions in aortic roots

Heart tissues containing the aortic roots were carefully dissected and fixed overnight in 4% PFA before embedding in Tissue-Tek optimal cutting temperature (OCT) compound (Sakura Finetek, Japan). To analyze the lesion area in the aortic root, OCT-embedded aortic roots were serially sectioned at 5 μm thickness through the aortic sinus with all 3 valve leaflets visible. Five sections at about 80-μm intervals per sample were analyzed by the H&E staining or Oil Red O staining to evaluate lesions throughout the aortic sinus. Quantitative analysis of lesion areas was performed with Image-Pro Plus 6.0 software.

Pulmonary hypertension mouse model

The tamoxifen-induced 6-week-old male *Mvp*^{ECKO} and *Mvp*^{ECWT} mice were exposed under normoxia (21% O_2 environment) or hypoxia (10% O_2) conditions regulated by an OxyCycler controller (BioSpherix) in a ventilated chamber for 3 weeks. Mice were anesthetized with isoflurane and placed on a heating pad. To measure right ventricular systolic pressure (RVSP), a 25-gauge needle connected to a pressure transducer was inserted into the right ventricle through the diaphragm. The tracings were recorded and analyzed by AcqKnowledge software (Biopac Systems). After the hemodynamic measurement, the heart was removed. RV was separated from the left ventricle and septum (LV + S) and weighted on an analytical balance. RV/(LV + S) weight ratio was represented as RV hypertrophy index. Murine lung samples were fixed with 4% PFA and embedded in OCT compound. Cross sections of 10 μm were prepared using a freezing microtome (CM-1950, LEICA) and stained with H&E. Vascular remodeling was quantified by measuring medial wall thickness using Image J (c1.48) software. Approximately 20 muscular arteries (25–50 μm in diameter) from lung were outlined randomly and blindly.

Immunofluorescence staining

Cultured cells were seeded on 4-well cell culture slides and fixed with 4% PFA for 15 min, followed by permeabilized in 0.1% Triton X-100 for 10 min. Cells were then blocked in 5% BSA, (prepared in 1× PBST) for 30 min at room temperature, and incubated with primary antibodies at 4 °C overnight. After washing in PBST three times, cells were incubated with Alexa Fluor-conjugated secondary antibodies for 1 h at room temperature in the dark. For immunofluorescence staining of tissue samples, serial cryosections were rehydrated in PBS, and sections were incubated with primary antibodies at 4 °C overnight, followed by Alexa Fluor-conjugated secondary antibodies for 2 h at room temperature in the dark. Nuclei were stained by mounting the slides with DAPI (4′,6-diamidino-2-phenylindole) medium (0100-20, SouthernBiotech). The staining was visualized with a fluorescence microscope or confocal laser scanning microscope (LSM900, Carl Zeiss, Germany). Immunofluorescence staining was performed using primary antibodies against MVP (1:100, sc-23916, Santa Cruz), CD31 (1:50, 550274, BD Biosciences), CD68 (1:200, MCA1957, Bio-Rad), α-SMA (1:200, A5228, Sigma-Aldrich), Parkin (1:100, 14060-1-AP, Proteintech), NEDD4L (1:50, sc-514954, Santa Cruz), Flag (F1804, 1:100, Sigma-Aldrich), LC3B (1:100, 2775, CST), and COXIV (1:200, 11967, CST). The secondary fluorescent antibodies were donkey anti-rat 488 (1:1000, A-21208, Invitrogen), donkey anti-rat 594 (1:1000, A-21209, Invitrogen), donkey anti-rabbit 488 (1:1000, A-21206, Invitrogen), donkey anti-rabbit 546 (1:1000, A10040, Invitrogen), donkey anti-rabbit 647 (1:1000, A-31573, Invitrogen), and donkey anti-mouse 555 (1:1000, A-31570, Invitrogen).

Immunohistochemistry

Human carotid plaques were fixed with 4% PFA before paraffin embedding. After deparaffinized and rehydrated, tissue sections

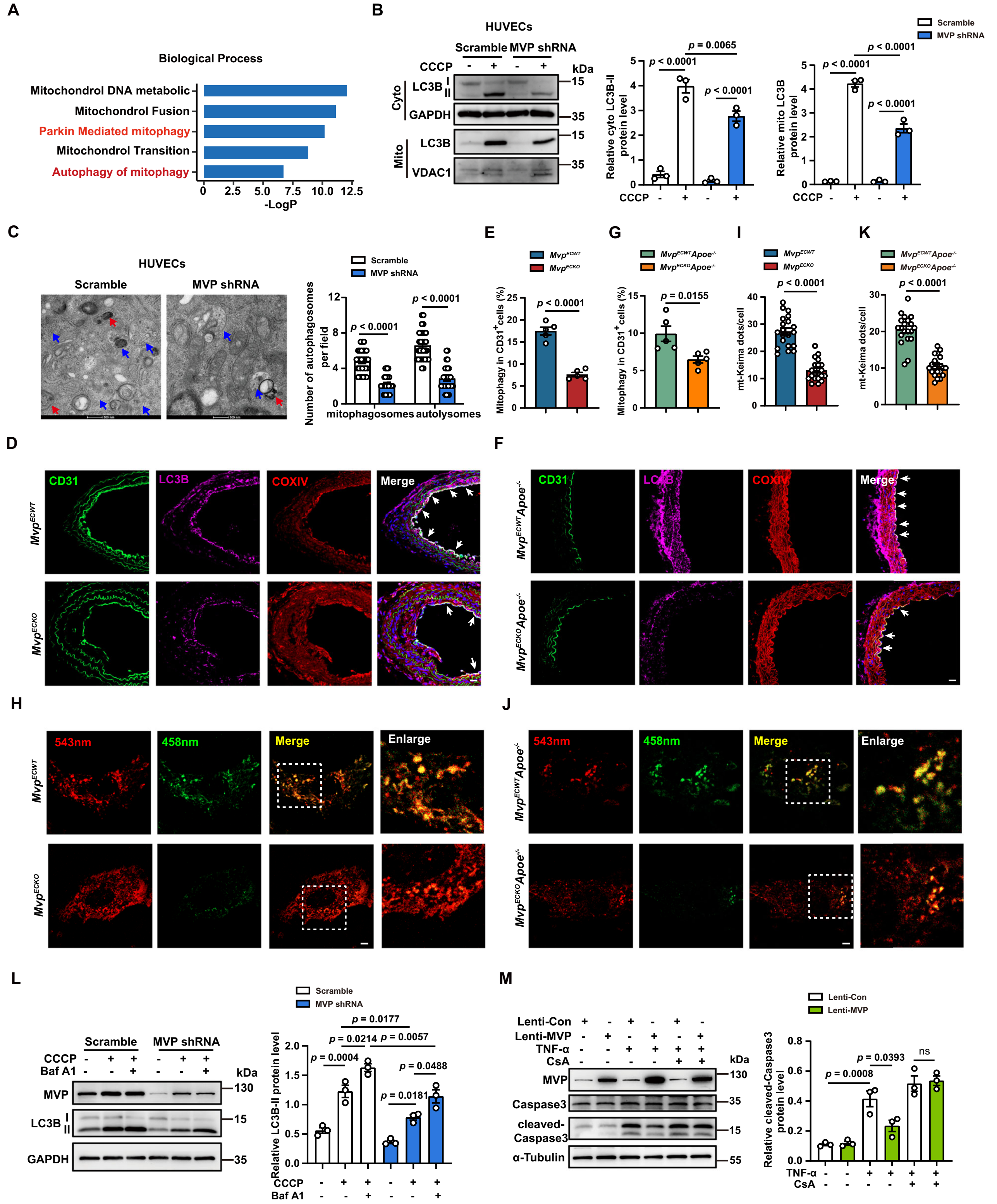

were treated with citrate antigen retrieval buffer and then incubated with 5% BSA blocking for 30 min at room temperature. The sections were then incubated with an anti-MVP antibody (1:100, sc-23916, Santa Cruz) at 4 °C overnight followed by incubation with an HRP-conjugated secondary antibody for 30 min and stained using a DAB solution. Images were visualized using a microscope (Carl Zeiss, Germany) and analyzed by Image-Pro Plus 6.0 software.

Cell cultures

Human aortic endothelial cells (HAECs, FC-0014) and human umbilical vein endothelial cells (HUVECs, FC-0003) were purchased from Lifeline Cell Technology and maintained in the endothelial cell medium (ECM, ScienCell Research Laboratories) supplemented with 5% fetal FBS, 1% penicillin/streptomycin (P/S), and 1% endothelial cell growth factors at 37 °C with 5% CO_2. Human lung microvascular endothelial cells (HLMECs, CTCC-001-HUM) were purchased from Zhejiang

Fig. 6 | MVP deficiency impairs mitophagy in ECs. A GO enrichment analysis of the downregulated DEGs in the HUVECs upon MVP knockdown. **B, C** MVP knockdown on mitophagy in the HUVECs treated by CCCP (10 μM) for 2 h. **B** Western blot analysis of autophagy protein LC3B in cytoplasmic and mitochondrial fractions of cells ($n = 3$, independent biological replicates). **C** Representative transmission electron microscope (TEM) images of the treated cells. Red arrows indicate mitophagosome vacuoles, and blue arrows indicate autolysosome vacuoles. Scale bars = 500 nm. The numbers of mitophagosome and autolysosome vacuoles per field were calculated ($n = 30$). **D, E** Spatial co-localization of mitochondrial protein COXIV (red) with LC3B (purple) in the CD31$^+$ ECs (green) of carotid arteries ligated for 7 days ($n = 5$). Scale bar = 20 μm. **F, G** Spatial co-localization of mitochondrial protein COXIV (red) with LC3B (purple) in the aortic CD31$^+$ ECs (green) after 4 weeks of WD feeding ($n = 5$). Scale bar = 20 μm. **H, I** Fluorescence staining of mKeima in the magnetic beads-sorted ECs of carotid arteries ligated for 7 day. Twenty cells per group ($n = 20$). Scale bar = 10 μm. **J, K** Fluorescence staining of mKeima in the magnetic beads-sorted ECs of aortas after 4 weeks of WD feeding. Twenty cells per group ($n = 20$). Scale bar = 10 μm. **L** MVP knockdown on LC3B expression in the HUVECs treated by Bafilomycin A1 (Baf-A1, 800 nM) and CCCP ($n = 3$, independent biological replicates). **M** MVP overexpression on Caspase3 and cleaved-Caspase3 expression in the HUVECs treated by cyclosporin A (CsA) (5 μM) and TNF-α (10 μg/ml) ($n = 3$, independent biological replicates). Data are presented as mean n ± SEM. Statistical significances are assessed by Mann-Whitney test (**C**), two-tailed Student's *t*-test (**E**, **G**, **I**, **K**), or one-way ANOVA followed by Tukey post hoc test (**B**, **L**, **M**). ns, no significance. Source data are provided as a Source Data file.

Meisen Cell Technology (China) and maintained in the ECM. Cell passages 3 to 7 were used in all experiments.

Mouse aortic endothelial cells (MAECs) were isolated from mouse aorta and cultured in ECM[56]. Briefly, aortas were collected and washed with PBS at 4 °C and then carefully stripped of fat and connective tissues. Aortas were cut into small segments and placed in Matrigel (Corning, 356234) with ECM. After 3-4 days, tissue segments were removed and the remaining MAECs were further cultured for up to 7 days. The identity of isolated ECs was confirmed by immunofluorescence staining using EC markers CD31. To re-expression MVP, *Mvp*$^{-/-}$ MAECs were transfection by lentivirus bearing MVP (Lenti-MVP) or control vector (Lenti-Con).

HEK293T cells (ATCC, CRL-3216) were cultured in the Dulbecco's Modified Eagle's Medium (DMEM)/F12 (Gibco) supplemented with 10% FBS (Gibco) and 1% P/S (Gibco). TNF-α (10291-TA) was from R&D Systems. Carbonyl cyanide 3-chloro-phenylhydrazone (CCCP, C2759) was purchased from Sigma-Aldrich. Cyclosporin A (CsA, HY-B0579), cycloheximide (CHX, HY-12320), and MG-132 (HY-13259) were purchased from MCE.

Plasmids and lentiviral production

EGFP-Parkin plasmid was purchased from YouBio (China). Human MVP, Parkin, and NEDD4L sequences were inserted into the pCDH (CMV-MCS) plasmid vector to generate recombinant Lenti-Flag-tagged-MVP, Lenti-HA-tagged-Parkin, and Lenti-Myc-tagged NEDD4L. The pLVX-U6-puro plasmid vector containing short hairpin RNAs (shRNAs) targeting human MVP (5'-GGTGCTGTTTGATGTCACA-3') and NEDD4L (5'-ACAAGATGATGTTGGGAAA-3') were purchased from GenePharma (China). Non-target negative scramble shRNA was used as a control. Lentiviral constructs were transfected by packaging and envelope plasmids to HEK293T cells. The recombinant lentivirus supernatant was harvested 72 h post-transfection, filtered through a 0.45 μm filter, and then added to the cultured cells in the media at a multiplicity of infection (MOI) of 10. Twenty-four hours after infection, the virus-containing media were replaced with fresh media. The knockdown or overexpression efficacy was determined at 72 h after transduction by western blot.

Analysis of endothelial apoptosis

Cell apoptosis was determined by flow cytometry (FACS Calibur, BD Biosciences) with an Annexin V/PI assay kit (Vazyme Biotech, China) according to the manufacturer's instructions. Representative graphs are shown after analysis with the FlowJo software. To analyze endothelial apoptosis in vivo, endothelial cell apoptosis in carotid arteries and thoracic aortas were detected by double stain with terminal deoxynucleotidyl transferase UTP nick end labeling (TUNEL) assay kit (G3250, Promega) and monoclonal anti-CD31 antibody (1:50, 550274, BD Biosciences).

In situ dihydroethidium (DHE) fluorescence staining

The DHE staining of mouse carotid arteries and thoracic aortas were conducted as previously described[57]. Briefly, the unfixed tissues were embedded in OCT and cut into 10-μm-thick sections. Serial cryosections were rehydrated in PBS. The aorta sections were immediately incubated with fresh 5 μM DHE staining solution for 30 min at 37 °C. After washing 3 times with PBS, the slides were mounted with DAPI medium (0100-20, SouthernBiotech), and images were captured with a fluorescence microscope (Scope A1, Carl Zeiss, Germany). Quantitative analysis of the DHE fluorescence within the aortic wall was performed with Image J (c1.48) software.

Measurement of cellular reactive oxygen species (ROS)

The intracellular ROS production was detected by labeling with dichlorofluorescin diacetate (DCFH-DA, S0033, Beyotime, China). Briefly, after treated with TNF-α (10 μg/ml) for 12 h, HUVECs and HAECs were washed with PBS and stained with DCFH-DA (10 μM) at 37 °C for 20 min. After three washes with PBS, ROS production was analyzed via flow cytometry (FACS Calibur, BD Biosciences). The averaging fluorescence intensity of outlined cells was analyzed using FlowJo (v10.6.2) software.

Measurement of mitochondrial ROS

For determination of intracellular mitochondrial ROS (mitoROS) in vitro, HUVECs and HAECs were incubated with MitoSOX (5 μM, M36005, ThermoFisher Scientific) probe for 20 min at 37 °C. After three washes with PBS, mitoROS production was analyzed under a confocal laser scanning microscope (LSM900, Carl Zeiss, Germany). The averaging fluorescence intensity of cells was analyzed using Image J (c1.48) software.

Measurement of mitochondrial membrane potential (MMP)

The mitochondrial membrane potential was measured by loading cells with fluorescent dye JC-1 (HY-15534, MCE). JC-1 is a fluorescent lipophilic carbocyanine dye used to measure mitochondrial membrane potential. When the mitochondrial membrane potential is high, JC-1 aggregates in the matrix to form JC aggregates that produce red fluorescence. When the mitochondrial membrane potential is low, JC-1 does not aggregate in the mitochondrial matrix. The presence of monomers produces green fluorescence. Briefly, following 20 min incubation with JC-1 (5 μM) for 30 min at 37 °C in the dark, the cells were washed twice with PBS. The green JC monomers (488 nm) and red JC aggregates (570 nm) were visualized by a fluorescence microscope (Carl Zeiss, Germany). Mean fluorescence intensity of cells was analyzed with Image J (c1.48) software.

Transmission electronic microscopy (TEM)

For TEM detection, HUVECs and HAECs treated with CCCP were trimmed into smaller pieces and fixed with 2% glutaraldehyde. Images were obtained using a TEM (FEI Tecnai G2) at 200 kV. Intracellular double-membrane vesicles containing mitochondria were identified as mitochondrial-autophagosomes, reflecting the level of mitophagy activity in the samples. The number of mitochondrial autophagosomes was calculated in 30 images per group.

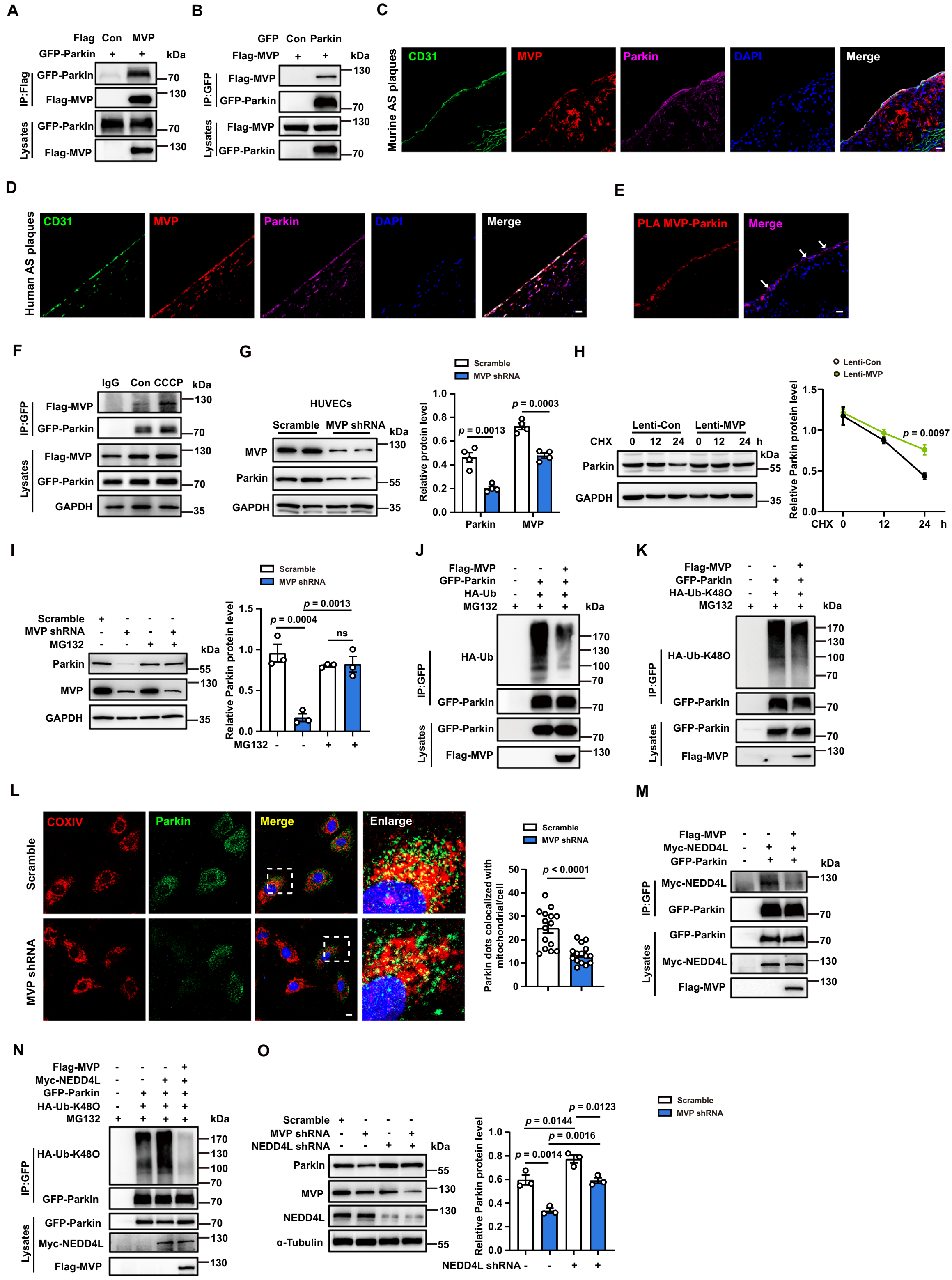

Assessment of mitophagy by mt-Keima

Mitophagy activity was assessed by immunofluorescence staining with the mt-Keima (a gift from Prof. Bei Liu, Chinese Academy of Sciences, Beijing, China)[24,25]. Under normal conditions, mt-Keima manifests green fluorescence. When mitophagy is induced, mitophagosomes fuse with lysosomes to form autolysosomes, and the pH will decrease and become acidic. Under acidic conditions, mt-Keima manifests red fluorescence. HUVECs seeded in a confocal dish were treated with CCCP (10 μM) for 2 h after being transfected with mt-Keima lentivirus for 48 h. For detection of mitophagy flux in vivo, Lenti-mKeima virus was intravenously injected into the ligated or WD-fed mice. Twenty-four hours later, carotid arteries and aortas were isolated. Endothelial cells were harvested by enzymatic digestion and CD31$^+$ magnetic bead sorting. The living cells were captured with a confocal microscope (LSM900, Carl Zeiss, Germany) and the quantity of mt-Keima dots within each cell was counted.

Fig. 7 | MVP stabilizes Parkin in endothelial cells. **A**, **B** Co-immunoprecipitation (Co-IP) of GFP-tagged Parkin (GFP-Parkin) and Flag-tagged MVP (Flag-MVP). HEK293T cells were co-transfected by GFP-Parkin and Flag-MVP. Cell lysates were immunoprecipitated by anti-Flag antibody and were immunoblotted by anti-GFP antibody (**A**), or immunoprecipitated by anti-GFP antibody and immunoblotted by anti-Flag antibody (**B**). **C**, **D** Co-localization staining of MVP (red) with Parkin (purple) in CD31$^+$ ECs (green) of murine (**C**) and human (**D**) atherosclerotic plaques. Scale bars = 20 μm. **E** Proximity ligation assay (PLA) indicating the interaction between MVP and Parkin (red dots) in murine atherosclerotic plaques. Scale bars = 20 μm. **F** Co-IP of GFP-Parkin and Flag-MVP in the HEK293T cells treated by CCCP (10 μM) for 30 min. **G** MVP knockdown on Parkin expression in HUVECs (*n* = 4, independent biological replicates). **H** MVP overexpression on Parkin expression in the HUVECs treated by cycloheximide (CHX) (*n* = 3, independent biological replicates). **I** MVP knockdown on Parkin expression in the HUVECs treated by 26S proteasome inhibitor MG132 (20 μM) for 6 h (*n* = 3, independent biological replicates). **J** Co-IP of GFP-Parkin, HA-Ub, and Flag-MVP in the HEK293T cells treated by MG132 (20 μM) for 6 h. **K** Co-IP of GFP-Parkin, HA-Ub-K48O, and Flag-MVP in the HEK293T cells treated by MG132 (20 μM) for 6 h. **L** Representative IF staining of Parkin (green), COXIV (red), and DAPI (blue) in the MVP knockdown HUVECs treated by CCCP for 2 h. Fifteen cells per group (*n* = 15). Scale bar = 20 μm. **M** Co-IP of GFP-Parkin, Myc-NEDD4L, and Flag-MVP in HEK293T cells. **N** Co-IP of GFP-Parkin, Myc-NEDD4L, HA-Ub-K48O, and Flag-MVP in the HEK293T cells treated by MG132 (20 μM) for 6 h. **O** Effects of MVP and NEDD4L knockdown on the Parkin expression in HUVECs (*n* = 3, independent biological replicates). Data are presented as mea*n* ± SEM. Statistical significances are assessed by two-tailed Student's *t*-test (**G**), two-way ANOVA with Bonferroni's multiple comparisons test (**H**), Mann-Whitney test (**L**), or one-way ANOVA followed by Tukey post hoc test (**I, O**). Experiments were repeated independently with similar results three times in A-F, J, K, M, and N. ns, no significance. Source data are provided as a Source Data file.

Mitochondria isolation

A mitochondria isolation kit was used for isolating mitochondrial fractions following the manufacturer's instruction (ThermoFisher Scientific). Briefly, cells were harvested and re-suspended in the mitochondria isolation reagent A. The lysis was vortexed and incubated on ice for 2 min before adding mitochondria isolation reagent B. After sufficient vortex and incubation, reagent C was added, and the mixture was centrifuged at 700 g for 10 min. The mitochondria were deposited in the pellet after the supernatant was centrifuged for 15 min at 12,000 g.

Co-immunoprecipitation (Co-IP) assay

Cells were lysed in immunoprecipitation buffer (P0013, Beyotime, China) with protease inhibitors and phosphatase inhibitors (Roche, Germany) for 30 min on ice. Cellular debris was then pelleted by centrifugation at 12,000 g for 15 min at 4 °C. One tenth volume of the supernatant was retained as input, and the remaining was incubated with the indicated primary antibody overnight on the rotator at 4 °C. On the next day, protein A/G agarose beads (sc-2003, Santa Cruz) were added to capture immune complexes at 4 °C for 4 h. After washing with lysis buffer 3 times, the immunocomplexes were eluted with 2×SDS loading buffer at 95 °C. The immunoprecipitated proteins were resolved by SDS-PAGE and blotted with the indicated antibody.

Proximity ligation assay (PLA)

PLA was performed with Duolink reagents (DUO92101, Sigma) following the manufacturer's instructions. Sections from murine atherosclerotic plaques were fixed with 4% PFA and then permeabilized with 0.1% Triton X-100 for 30 min followed by blocking with Duolink blocking buffer for 1 h. Primary antibodies against MVP (sc-101266, Santa Cruz Biotechnology), Parkin (ab81321, Proteintech), and/or NEDD4L (sc-5307, Santa Cruz Biotechnology) were then incubated overnight at 4 °C. After washing, exact Rabbit PLUS and Mouse MINUS probes conjugated with secondary antibodies were added and hybridized for 1 h at 37 °C. Ligation, rolling circle amplification, and detection with fluorescent probes were performed. PLA signals, recognized as red fluorescent dots, were captured by confocal microscopy (LSM900, Carl Zeiss, Germany). Negative controls were performed using IgG.

Western blot analysis

Cells were harvested and lysed in radioimmunoprecipitation (RIPA) lysis buffer supplemented with protease inhibitors and phosphatase inhibitors (Roche, Germany). Total cell lysates were subjected to sodium dodecyl sulfate-polyacrylamide gel electrophoresis (SDS-PAGE) and transferred to polyvinylidene difluoride (PVDF) membrane (Millipore, USA). After blocking for 1 h at room temperature in Tris-buffered saline (TBS) containing 0.05% Tween-20 (TBST) and 5% BSA, membranes were then incubated with primary antibody overnight at 4 °C. The sources of primary antibodies used are listed in the Supplementary table 2. After washing, the membranes were incubated with corresponding horseradish-peroxidase (HRP)-conjugated secondary antibodies and visualized with the ECL chemiluminescence detection kit (Pierce) in the ChemiDoc XRS$^+$ imaging system (BioRad). Image J (c1.48) software was used to quantify western blot image data.

Total RNA extraction and real-time qPCR analysis

Total RNA was extracted from cells using RNAiso Plus (TaKaRa, Japan) and subjected to complementary DNA synthesis using commercial kits (Vazyme Biotech, China) according to the manufacturer's instructions. Real-time qPCR (RT-qPCR) was performed in the ABI 7500 Real-Time PCR System (Life Technologies) using gene-specific primers and SYBR qPCR Master Mix (Vazyme Biotech, China). The results were normalized to the GAPDH level, and the fold change was determined using the $2^{-\Delta\Delta CT}$ method. The primer sequences in this study are as follows: human Parkin (Forward: 5'-GTGTTTGTCAGGTTCAACTCCA-3'; Reverse: 5'-GAAAATCACACGCAACTGGTC-3') and human GAPDH (Forward: 5'-GAAAATCACACGCAACTGGTC-3'; Reverse: 5'-CTCGCTCCTGG AAGA TGGTGATGG-3').

RNA sequencing (RNA-seq)

HUVECs transduced by MVP shRNA and Scramble shRNA lentivirus were treated with TNF-α (10 ng/ml) for 8 h. After treatment, total RNAs were isolated from HUVECs with RNAiso Plus (TaKaRa, Japan). RNA-seq analysis was performed using a BGISEQ-500 apparatus (BGI, China). Differentially expressed genes (DEGs) were identified using DESeq2 with fold change > 2 and FDR < 0.05. Gene Ontology (GO) enrichment analysis was conducted using the R packages "Clusterprofile". The raw RNA-seq data have been deposited in the Genome Sequence Archive (GSA) for Human at the National Genomics Data Center (Beijing, China) under accession code HRA010306.

Analysis of the publicly available human atherosclerotic plaque transcriptome

From the NCBI GEO database, we collected human atherosclerotic plaque datasets spanning atherosclerosis (GSE100927, GSE443292, and GSE28829). MVP expression was compared between healthy controls and patients with carotid plaques. Gene co-expression network analysis (WGCNA) was conducted by R package "WGCNA".

Statistical analysis

Statistical analysis was performed using GraphPad Prism 8.0 software. Data are presented as mea*n* ± SEM. All data were evaluated for normality and variance. For normally distributed data, unpaired two-tailed

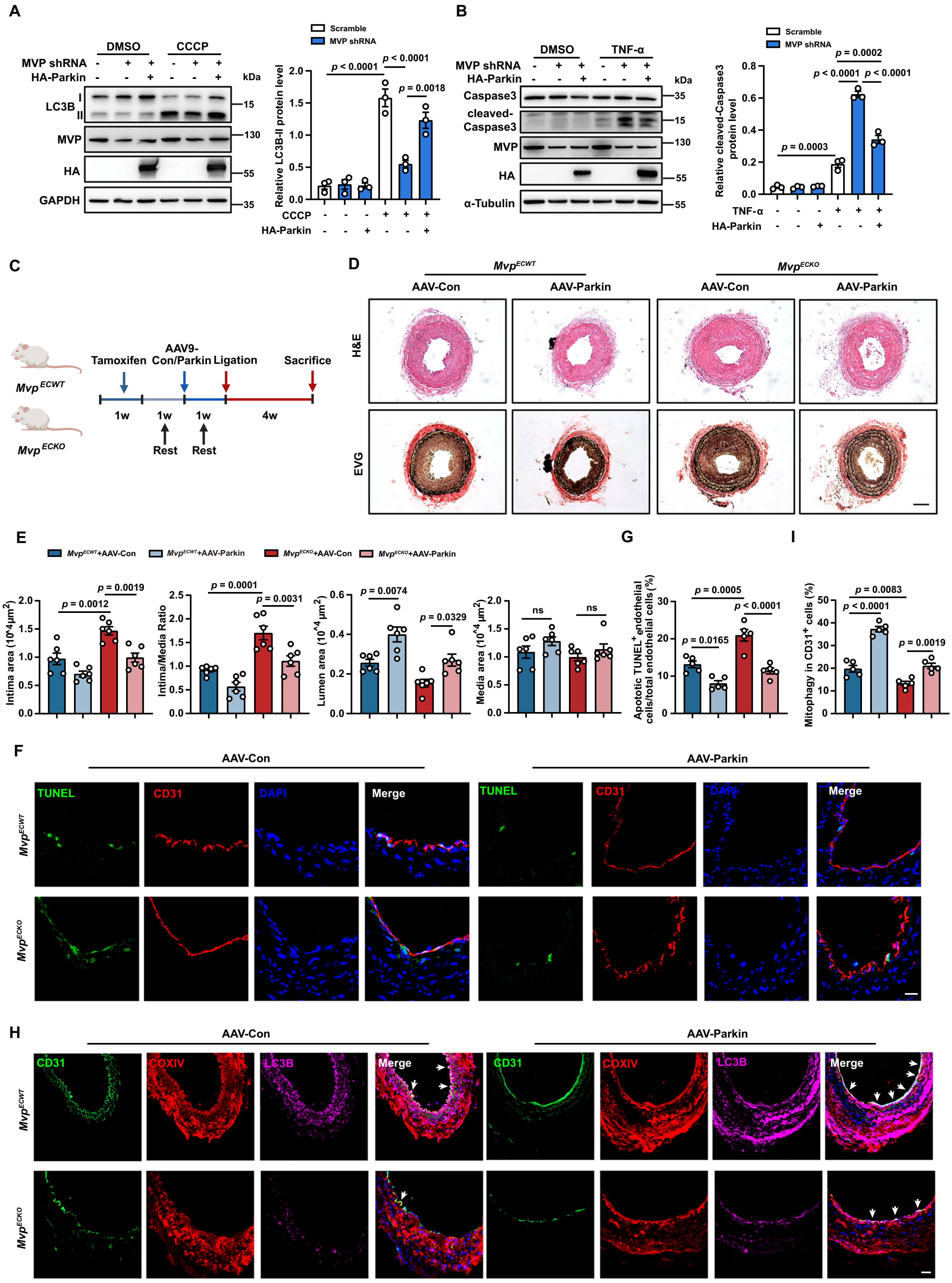

Student's *t*-test was used to compare the difference between 2 groups, and one-way ANOVA followed by Tukey's post hoc analysis was used for comparison among 3 or more groups. For data that were not normally distributed, nonparametric tests, Mann-Whitney non-parametric analysis (two-group analysis) or Kruskal-Wallis non-parametric test was used, followed by Dunn multiple comparison. $P < 0.05$ was considered statistically significant. All results are representative of at least 3 independent experiments.

Reporting summary

Further information on research design is available in the Nature Portfolio Reporting Summary linked to this article.

Fig. 8 | Parkin overexpression rescues MVP deficiency-induced endothelial apoptosis and mitophagy arrest. A Parkin overexpression on LC3B expression in the MVP knockdown HUVECs treated by CCCP (10 μM) ($n = 3$, independent biological replicates). **B** Parkin overexpression on Caspase3 and cleaved-Caspase3 expression in the MVP knockdown HUVECs treated by TNF-α (10 μg/ml) ($n = 3$, independent biological replicates). **C** Schematic illustration of Parkin overexpression in carotid artery-ligated *Mvp*^{ECKO} mice. Six-week-old male *Mvp*^{ECWT} and *Mvp*^{ECKO} mice were intravenously injected by the EC-driven adeno-associated virus (AAV) vector encoding Parkin after tamoxifen induction. Seven days after AAV injection, left common carotid arteries were ligated for 28 days. The figure is created using BioRender. Jiang B. (2025) https://BioRender.com/r5jpwb7. **D** Representative H&E and EVG staining images of the ligated carotid arteries. Scale bar, 50 μm. **E** Quantifications of neointima area, intima to media ratio, lumen area, and media area of ligated carotid arteries in (**D**) ($n = 6$). **F** Representative images of TUNEL and CD31 staining of the ligated carotid arteries. Scale bars, 20 μm. **G** Percentage of apoptotic ECs in total ECs in the ligated carotid arteries ($n = 5$). **H** Representative IF staining images of COXIV (red), LC3B (purple), and CD31$^+$ ECs (green) in the ligated carotid arteries. Scale bar = 20 μm. **I** Percentage of LC3B$^+$COXIV$^+$ ECs in total ECs in the ligated carotid arteries ($n = 5$). Data are presented as mean ± SEM. Statistical significances are assessed by one-way ANOVA followed by Tukey post hoc test (**A**, **B**, **E**, **G**, **I**). ns, no significance. Source data are provided as a Source Data file.

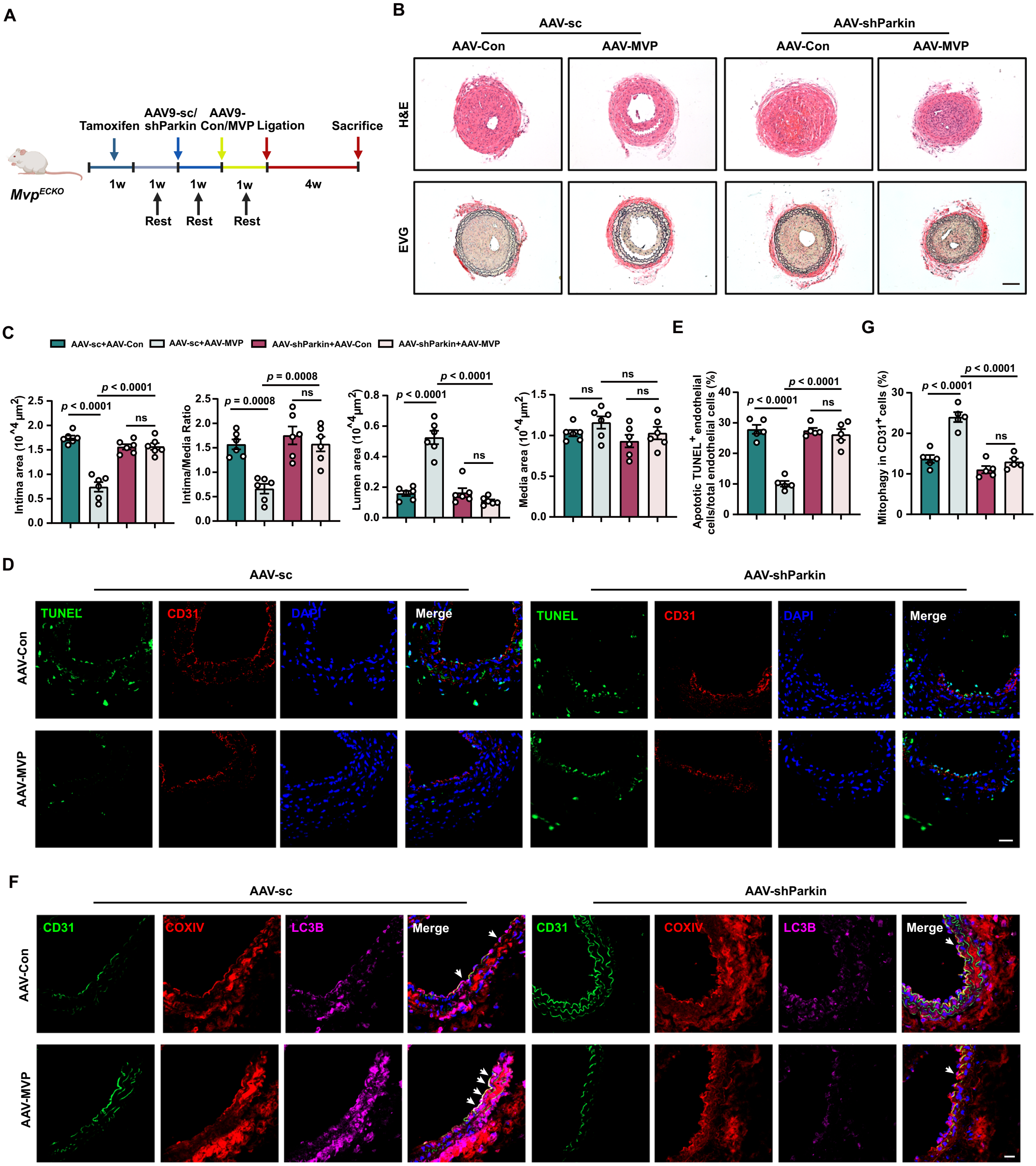

Fig. 9 | The protective effect of endothelial MVP overexpression against vascular remodeling depends on Parkin. **A** Schematic illustration of genetical modulation of Parkin on the ligation-induced vascular remodeling in *Mvp*^{ECKO} mice. Six-week-old male *Mvp*^{ECKO} mice were intravenously injected by the EC-driven AAV-shParkin after tamoxifen induction. Following 7 days, mice were intravenously injected by the EC-driven AAV-MVP to re-express endothelial MVP. Seven days later, left common carotid arteries were ligated for 28 days. The figure is created using BioRender. Jiang B. (2025) https://BioRender.com/exkw1l1. **B** Representative H&E and EVG staining images of the ligated carotid arteries. **C** Quantifications of neointima area, intima to media ratio, lumen area, and media area of ligated carotid arteries in mice ($n = 6$). Scale bar = 50 µm. **D** Representative staining images of TUNEL and CD31 in carotid arteries. Scale bars, 20 µm. **E** Percentage of apoptotic ECs in total ECs in the ligated carotid arteries ($n = 5$). **F** Representative IF staining images of COXIV (red), LC3B (purple), and CD31$^+$ ECs (green) in the ligated carotid arteries. Scale bar = 20 µm. **G** Percentage of LC3B$^+$COXIV$^+$ ECs in total ECs in the ligated carotid arteries ($n = 5$). Data are presented as mean ± SEM. Statistical significances are assessed by one-way ANOVA followed by Tukey post hoc test (**C**, **E**, **G**). ns no significance. Source data are provided as a Source Data file.

Data availability

Data generated in this study are provided in the Source Data file. The raw sequencing data for scRNA-seq generated in this study have been deposited at the Genome Sequence Archive (GSA) at the National Genomics Data Center (Beijing, China) under accession code CRA022574. The raw bulk RNA-seq data generated in this study have been deposited in the GSA for Human at the National Genomics Data Center (Beijing, China) under accession code HRA010306. Additionally, three publicly available RNA-seq datasets of human atherosclerotic plaques are from the Gene Expression Omnibus (GEO) under accession codes GSE100927, GSE43292, and GSE28829. The remaining data are available within the Article, Supplementary Information, or Source Data file. Source data are provided with this paper.

Code availability

The code was based on the official tutorials of the packages listed, no custom code was generated.

References

1. Libby, P. et al. Atherosclerosis. *Nat. Rev. Dis. Prim.* **5**, 56 (2019).
2. Gibbons, G. H. & Dzau, V. J. The emerging concept of vascular remodeling. *N. Engl. J. Med* **330**, 1431–1438 (1994).
3. Karimi Galougahi, K., Ashley, E. A. & Ali, Z. A. Redox regulation of vascular remodeling. *Cell Mol. Life Sci.* **73**, 349–363 (2016).
4. Davignon, J. & Ganz, P. Role of endothelial dysfunction in atherosclerosis. *Circulation* **109**, Iii27–Iii32 (2004).
5. Vargas, J. N. S., Hamasaki, M., Kawabata, T., Youle, R. J. & Yoshimori, T. The mechanisms and roles of selective autophagy in mammals. *Nat. Rev. Mol. Cell Biol.* **24**, 167–185 (2023).
6. Wang, S. et al. The mitophagy pathway and its implications in human diseases. *Signal Transduct. Target Ther.* **8**, 304 (2023).
7. Dymkowska, D. The involvement of autophagy in the maintenance of endothelial homeostasis: The role of mitochondria. *Mitochondrion* **57**, 131–147 (2021).
8. Gatica, D., Chiong, M., Lavandero, S. & Klionsky, D. J. The role of autophagy in cardiovascular pathology. *Cardiovasc Res* **118**, 934–950 (2022).
9. Scheffer, G. L. et al. The drug resistance-related protein LRP is the human major vault protein. *Nat. Med.* **1**, 578–582 (1995).
10. Chung, J. H., Ginn-Pease, M. E. & Eng, C. Phosphatase and tensin homologue deleted on chromosome 10 (PTEN) has nuclear localization signal-like sequences for nuclear import mediated by major vault protein. *Cancer Res* **65**, 4108–4116 (2005).
11. Li, S. et al. Zebrafish MVP recruits and degrades TBK1 to suppress IFN production. *J. Immunol.* **202**, 559–566 (2019).
12. Kolli, S., Zito, C. I., Mossink, M. H., Wiemer, E. A. & Bennett, A. M. The major vault protein is a novel substrate for the tyrosine phosphatase SHP-2 and scaffold protein in epidermal growth factor signaling. *J. Biol. Chem.* **279**, 29374–29385 (2004).
13. Das, D., Wang, Y. H., Hsieh, C. Y. & Suzuki, Y. J. Major vault protein regulates cell growth/survival signaling through oxidative modifications. *Cell Signal* **28**, 12–18 (2016).
14. Qi, Y. et al. Major vault protein attenuates cardiomyocyte injury in doxorubicin-induced cardiomyopathy through activating AKT. *BMC Cardiovasc Disord.* **22**, 77 (2022).
15. Ben, J. et al. Major vault protein suppresses obesity and atherosclerosis through inhibiting IKK-NF-κB signaling mediated inflammation. *Nat. Commun.* **10**, 1801 (2019).
16. Liu, Q. et al. Major Vault Protein Prevents Atherosclerotic Plaque Destabilization by Suppressing Macrophage ASK1-JNK Signaling. *Arterioscler Thromb. Vasc. Biol.* **42**, 580–596 (2022).
17. Su, M. et al. Endothelial IGFBP6 suppresses vascular inflammation and atherosclerosis. *Nat. Cardiovasc. Res.* **4**, 145–162 (2025).
18. Pan, H. et al. Single-Cell Genomics Reveals a Novel Cell State During Smooth Muscle Cell Phenotypic Switching and Potential Therapeutic Targets for Atherosclerosis in Mouse and Human. *Circulation* **142**, 2060–2075 (2020).
19. Li, F. et al. Single-cell RNA-seq reveals cellular heterogeneity of mouse carotid artery under disturbed flow. *Cell Death Discov.* **7**, 180 (2021).
20. Andueza, A. et al. Endothelial Reprogramming by Disturbed Flow Revealed by Single-Cell RNA and Chromatin Accessibility Study. *Cell Rep.* **33**, 108491 (2020).
21. Shi, G. et al. Single-Cell Transcriptome Analysis Reveals Dynamic Populations of Vascular Cells in Neointimal Hyperplasia. *Front Biosci (Landmark Ed)* **29**, 173 (2024).
22. Vanlandewijck, M. et al. A molecular atlas of cell types and zonation in the brain vasculature. *Nature* **554**, 475–480 (2018).
23. Kalluri, A. S. et al. Single-Cell Analysis of the Normal Mouse Aorta Reveals Functionally Distinct Endothelial Cell Populations. *Circulation* **140**, 147–163 (2019).
24. Sun, N. et al. Measuring In Vivo Mitophagy. *Mol. Cell* **60**, 685–696 (2015).
25. Wu, H. et al. Defective mitochondrial ISCs biogenesis switches on IRP1 to fine tune selective mitophagy. *Redox Biol.* **36**, 101661 (2020).
26. Mauvezin, C. & Neufeld, T. P. Bafilomycin A1 disrupts autophagic flux by inhibiting both V-ATPase-dependent acidification and Ca-P60A/SERCA-dependent autophagosome-lysosome fusion. *Autophagy* **11**, 1437–1438 (2015).
27. Steiner, E. et al. The major vault protein is responsive to and interferes with interferon-gamma-mediated STAT1 signals. *J. Cell Sci.* **119**, 459–469 (2006).
28. Lange, C., Walther, W., Schwabe, H. & Stein, U. Cloning and initial analysis of the human multidrug resistance-related MVP/LRP gene promoter. *Biochem Biophys. Res Commun.* **278**, 125–133 (2000).
29. Zhu, L., Wang, F., Yang, H., Zhang, J. & Chen, S. Low shear stress damages endothelial function through STAT1 in endothelial cells (ECs). *J. Physiol. Biochem* **76**, 147–157 (2020).
30. Chien, S., Li, S. & Shyy, Y. J. Effects of mechanical forces on signal transduction and gene expression in endothelial cells. *Hypertension* **31**, 162–169 (1998).
31. Kluge, M. A., Fetterman, J. L. & Vita, J. A. Mitochondria and endothelial function. *Circ. Res* **112**, 1171–1188 (2013).
32. Torisu, K. et al. Intact endothelial autophagy is required to maintain vascular lipid homeostasis. *Aging Cell* **15**, 187–191 (2016).
33. Vion, A. C. et al. Autophagy is required for endothelial cell alignment and atheroprotection under physiological blood flow. *Proc. Natl Acad. Sci. USA* **114**, E8675–e8684 (2017).

34. Qian, X. et al. Enhanced Autophagy in GAB1-Deficient Vascular Endothelial Cells Is Responsible for Atherosclerosis Progression. *Front Physiol.* **11**, 559396 (2020).
35. Ge, P., Dawson, V. L. & Dawson, T. M. PINK1 and Parkin mitochondrial quality control: a source of regional vulnerability in Parkinson's disease. *Mol. Neurodegener.* **15**, 20 (2020).
36. Wu, L., Wang, L., Du, Y., Zhang, Y. & Ren, J. Mitochondrial quality control mechanisms as therapeutic targets in doxorubicin-induced cardiotoxicity. *Trends Pharm. Sci.* **44**, 34–49 (2023).
37. Ziviani, E., Tao, R. N. & Whitworth, A. J. Drosophila parkin requires PINK1 for mitochondrial translocation and ubiquitinates mitofusin. *Proc. Natl Acad. Sci. USA* **107**, 5018–5023 (2010).
38. Harper, J. W., Ordureau, A. & Heo, J. M. Building and decoding ubiquitin chains for mitophagy. *Nat. Rev. Mol. Cell Biol.* **19**, 93–108 (2018).
39. Li, P. et al. NR4A1 contributes to high-fat associated endothelial dysfunction by promoting CaMKII-Parkin-mitophagy pathways. *Cell Stress Chaperones* **23**, 749–761 (2018).
40. He, L. et al. PINK1/Parkin-mediated mitophagy promotes apelin-13-induced vascular smooth muscle cell proliferation by AMPKα and exacerbates atherosclerotic lesions. *J. Cell Physiol.* **234**, 8668–8682 (2019).
41. Wu, W. et al. PINK1-Parkin-Mediated Mitophagy Protects Mitochondrial Integrity and Prevents Metabolic Stress-Induced Endothelial Injury. *PLoS One* **10**, e0132499 (2015).
42. Onat, U. I. et al. Intercepting the Lipid-Induced Integrated Stress Response Reduces Atherosclerosis. *J. Am. Coll. Cardiol.* **73**, 1149–1169 (2019).
43. Wang, L., Qi, H., Tang, Y. & Shen, H. M. Post-translational Modifications of Key Machinery in the Control of Mitophagy. *Trends Biochem Sci.* **45**, 58–75 (2020).
44. Yu, F. & Zhou, J. Parkin is ubiquitinated by Nrdp1 and abrogates Nrdp1-induced oxidative stress. *Neurosci. Lett.* **440**, 4–8 (2008).
45. Niu, K. et al. USP33 deubiquitinates PRKN/parkin and antagonizes its role in mitophagy. *Autophagy* **16**, 724–734 (2020).
46. Shiiba, I. et al. MITOL promotes cell survival by degrading Parkin during mitophagy. *EMBO Rep.* **22**, e49097 (2021).
47. Huang, Z., Zhao, J., Wang, W., Zhou, J. & Zhang, J. Depletion of LncRNA NEAT1 Rescues Mitochondrial Dysfunction Through NEDD4L-Dependent PINK1 Degradation in Animal Models of Alzheimer's Disease. *Front Cell Neurosci.* **14**, 28 (2020).
48. Nazio, F. et al. Fine-tuning of ULK1 mRNA and protein levels is required for autophagy oscillation. *J. Cell Biol.* **215**, 841–856 (2016).
49. Lee, D. E. et al. NEDD4L downregulates autophagy and cell growth by modulating ULK1 and a glutamine transporter. *Cell Death Dis.* **11**, 38 (2020).
50. Ferro, I. et al. The human vault RNA enhances tumorigenesis and chemoresistance through the lysosome in hepatocellular carcinoma. *Autophagy* **18**, 191–203 (2022).
51. Horos, R. et al. The Small Non-coding Vault RNA1-1 Acts as a Riboregulator of Autophagy. *Cell* **176**, 1054–1067.e1012 (2019).
52. Kumar, A. & Lindner, V. Remodeling with neointima formation in the mouse carotid artery after cessation of blood flow. *Arterioscler Thromb. Vasc. Biol.* **17**, 2238–2244 (1997).
53. Li, Z. et al. Short AIP1 (ASK1-Interacting Protein-1) Isoform Localizes to the Mitochondria and Promotes Vascular Dysfunction. *Arterioscler Thromb. Vasc. Biol.* **40**, 112–127 (2020).
54. Xiao, W. et al. Recombinant DTβ4-inspired porous 3D vascular graft enhanced antithrombogenicity and recruited circulating CD93(+)/CD34(+) cells for endothelialization. *Sci. Adv.* **8**, eabn1958 (2022).
55. Daugherty, A. et al. Recommendation on Design, Execution, and Reporting of Animal Atherosclerosis Studies: A Scientific Statement From the American Heart Association. *Arterioscler Thromb. Vasc. Biol.* **37**, e131–e157 (2017).
56. Wang, J. M., Chen, A. F. & Zhang, K. Isolation and Primary Culture of Mouse Aortic Endothelial Cells. *J. Vis. Exp.* **118**, 52965 (2016).
57. Meng, B. et al. Myeloid-derived growth factor inhibits inflammation and alleviates endothelial injury and atherosclerosis in mice. *Sci. Adv.* **7**, eabe6903 (2021).

Acknowledgements

Thanks to Professor Yong Xu (Nanjing Medical University) and Bei Liu (Chinese Academy of Sciences) for providing us the *Cdh5*-Cre^{ERT2} mice and mt-Keima plasmid, respectively. We also thank Professor Xin Guo, Jie Wang, and Feng Chen (Nanjing Medical University) for their technical supports. This work was supported by grants from the National Natural Science Foundation of China (No. 82430018, 82030012 to Q.C.; No.82100433 to B.J.; No. 82470439, 82270476, 82070457 to J.J.B.; No. 82170444 to X.D.Z.; 82300515 to D.D.W.), the Natural Science Foundation of the Jiangsu Higher Education Institutions of China (23KJA310001 to B.J.; 20KJA310007 to X.D.Z.).

Author contributions

Q.C., J.J.B., and B.J. conceived and designed the work. B.J., F.B., Y.F.H., Y.R., Y.S., W.X.S., K.X.X, J.L.P., Y.Y.L., and Y.X.F. performed research, collected and analyzed the data. X.X.L., H.W.Z., X.D.Z., H.B., and Q.Y. provided technical assistances. B.J., J.J.B., and Q.C. wrote the paper. All authors read and approved the final manuscript.

Competing interests

The authors declare no competing interests.

Additional information

Supplementary information The online version contains supplementary material available at https://doi.org/10.1038/s41467-025-59644-y.

Correspondence and requests for materials should be addressed to Bin Jiang, Jingjing Ben or Qi Chen.

Peer review information *Nature Communications* thanks Jun Ren, and the other, anonymous, reviewer(s) for their contribution to the peer review of this work. A peer review file is available.